Reprinted from
Atmospheric Processes Over Complex Terrain
Meteorological Monographs, Vol. 23, No. 45,
June 1990
American Meteorological Society

Mountain Waves and Downslope Winds

DALE R. DURRAN

Department of Atmospheric Sciences, University of Washington, Seattle, Washington

ABSTRACT

In an effort to enhance the reader's physical understanding, this chapter begins with a discussion of fundamental concepts including parcel oscillations in a stable atmosphere, wave propagation, and the fluid motions associated with vertically propagating internal gravity waves. This is followed by a brief review of the theory of small-amplitude mountain waves, beginning with the case of air flowing over a series of sinusoidal ridges in a basic state with uniform wind speed and stability. The linear theory is then extended to cover isolated mountains and situations with vertical variations in the basic-state wind speed and stability.

The effects of nonlinearity on the flow are introduced in a discussion of downslope windstorms. Three different theoretical models of the downslope windstorm are compared. The first argues that the development of strong downslope winds is analogous to the transition from subcritical to supercritical flow in a hydraulic jump. The second proposes that downslope winds are produced by the superposition of partially reflected waves generated at atmospheric interfaces where there is a rapid change in the static stability, such as the tropopause. The third suggests that strong winds are produced by processes that become active when vertically propagating waves become unstable and "break" in the upper troposphere.

The problem of forecasting downslope winds is discussed. Recent observational and theoretical investigations of the gust structure embedded in the downslope wind current are reviewed. The paper concludes with a selective overview of recent work on the flow around isolated three-dimensional mountains.

4.1. Introduction

A disturbance is created when stably stratified air is forced to rise over a topographic barrier. The energy associated with that disturbance is usually carried away from the mountain by gravity waves. Gravity waves forced by mountains are specifically referred to as *mountain waves*. Mountain waves exert a drag on the upper levels of the atmosphere; indeed, the cumulative worldwide effect of mountain-wave drag is believed to have a significant influence on the strength of the mean zonal circulation near the polar jet streams. Large-amplitude mountain waves can be associated with regions of clear-air turbulence that pose a hazard to aviation. Mountain waves can also be associated with strong surface winds that blow down the mountain along its lee slope; wind gusts in excess of 50 m s^{-1} have been measured in extreme events.

This chapter reviews some of the fundamental aspects of mountain waves and examines recent progress in our understanding of downslope windstorms and the airflow around an isolated mountain. A discussion of the basic physical properties of internal gravity waves is provided in section 4.2, and is intended to improve the reader's physical intuition about the motions in these waves. Although the material in section 4.2 is certainly elementary, it is not often covered in textbooks [Gill (1982) is the exception]. The theory of section 4.2 is applied to linear mountain waves in section 4.3. Detailed expositions of linear mountain-wave theory have been provided by a number of previous authors; therefore, section 4.3 is limited to a brief review. Downslope windstorms are discussed in section 4.4; this material draws on a number of recent studies that appear to have clarified our understanding of the dynamics governing these events. Recent progress in our understanding of the airflow over an isolated mountain is described in section 4.5.

4.2. Fundamentals of internal gravity waves

While most people have some intuitive familiarity with external gravity waves through their contact with surface water waves, many meteorologists are not familiar with the atmospheric motions that occur in an internal gravity wave. Therefore, in an attempt to gain a more thorough physical understanding of mountain waves, let us review some fundamental aspects of gravity waves. For simplicity, the influence of the Coriolis force will be neglected and the waves will be assumed to lie in the two-dimensional x–z plane.

The basic forces that give rise to internal gravity waves are buoyancy restoring forces. If an air parcel is displaced vertically in a stably stratified flow, the buoyancy difference between the parcel and its environment will produce a restoring force, accelerating the parcel back toward its equilibrium position. In the absence of pressure gradient

forces, the parcel will oscillate along a vertical axis through its equilibrium position at the Brunt–Väisälä frequency

$$N = \left(\frac{g}{\theta_0}\frac{d\theta_0}{dz}\right)^{1/2}, \tag{4.1}$$

where $\theta_0(z)$ is the vertically varying mean-state potential temperature. [The derivation of this result may be found in Holton (1979) p. 50, or Gill (1982) p. 129.] If pressure gradient forces are again neglected and the parcel is constrained to oscillate along a path tilted off the vertical axis by an angle ϕ (one might imagine that it is attached to a slanted rod by a frictionless coupling), buoyancy forces will produce an identical type of oscillatory motion at the reduced frequency $N\cos\phi$. The factor $\cos\phi$ arises from the reduction in the component of gravitational acceleration, and the reduction in the apparent stratification, along the slanting path [see Holton (1979) p. 160, or Gill (1982) p. 132]. Thus, buoyancy driven oscillations can be accommodated at any frequency less than N by selecting a suitable angle for the sloping trajectory. However, it is not possible to support buoyancy driven parcel oscillations at frequencies greater than the Brunt–Väisälä frequency.

The pressure gradients and buoyancy forces in an internal gravity wave play the role of the slanting rod with the frictionless coupling in the preceding illustration—they act in concert to keep air parcels oscillating along a path slanted off-vertical at the angle that matches the frequency of the wave to the resonant frequency $N\cos\phi$. In order to see how this works, consider small-amplitude perturbations about a basic state at rest in a Boussinesq atmosphere, which satisfy the linearized governing equations

$$\frac{\partial u}{\partial t} + \frac{\partial P}{\partial x} = 0, \tag{4.2}$$

$$\frac{\partial w}{\partial t} + \frac{\partial P}{\partial z} = b, \tag{4.3}$$

$$\frac{\partial b}{\partial t} + N^2 w = 0, \tag{4.4}$$

$$\frac{\partial u}{\partial x} + \frac{\partial w}{\partial z} = 0, \tag{4.5}$$

where $b = g(\theta - \theta_0)/\theta_s$, $P = c_p\theta_s(\pi - \pi_0)$, and $N^2 = (g/\theta_s)d\theta_0/dz$ [the Boussinesq version of Eq. (4.1)]. Here π is the Exner function pressure $(p/p_s)^{R/c_p}$; $\pi_0(z)$ and $\theta_0(z)$ are the hydrostatically balanced basic-state pressure and potential temperature; p_s and θ_s are constant reference values, and b represents buoyancy. Equations (4.2)–(4.5) are formally equivalent to the linearized Boussinesq equations for an incompressible fluid (for which $b = -g(\rho - \rho_0)/\rho_s$, $P = (p - p_0)/\rho_s$, and $N^2 = -(g/\rho_s)d\rho_0/dz$). These equations reduce to a single equation for w:

$$\frac{\partial^2}{\partial t^2}\left[\frac{\partial^2}{\partial x^2} + \frac{\partial^2}{\partial z^2}\right]w + N^2\frac{\partial^2 w}{\partial x^2} = 0. \tag{4.6}$$

A solution to (4.6), describing the vertical velocity perturbations in an internal gravity wave, is

$$w = w_0\cos(kx + mz - \nu t). \tag{4.7}$$

Given the preceding expression for w, (4.5) implies

$$u = -\frac{m}{k}w_0\cos(kx + mz - \nu t), \tag{4.8}$$

and (4.4) requires

$$b = \frac{N^2}{\nu}w_0\sin(kx + mz - \nu t). \tag{4.9}$$

Finally, (4.2) and (4.8) imply

$$P = -\frac{\nu m}{k^2}w_0\cos(kx + mz - \nu t). \tag{4.10}$$

A schematic diagram is plotted in Fig. 4.1, representing the perturbation fields (4.7)–(4.10) at a single instant in time. All perturbation quantities are constant along the straight lines $kx + mz$ = constant; these are lines of constant phase, or "wave fronts." Equations (4.7) and (4.8) imply that $u/w = -m/k$; thus *all air parcel motions are parallel to the wave fronts.* The angle between the slanting air parcel trajectories and the vertical (ϕ) is determined by the dispersion relation

$$\nu^2 = \frac{N^2k^2}{k^2 + m^2} = N^2\cos^2\phi. \tag{4.11}$$

It follows that the air parcels in an internal gravity wave oscillate along trajectories exactly as if they were attached to a rod slanting off the vertical at the angle $\phi = \cos^{-1}(\nu/N)$.

The case illustrated in Fig. 4.1 is one in which $k < 0$ and $m < 0$ (ν is assumed greater than zero by convention, in order to eliminate redundant solutions). The slanting solid lines in Fig. 4.1 represent those lines of constant phase where the perturbation velocities reach their extrema; the direction of the velocity along each of these lines is indicated by open arrows. These lines are also the location of the extrema in the pressure field, and are labeled as required by (4.10). The perturbation velocities and pressure are zero along the dashed wave fronts. Equation (4.9) shows that, when $k < 0$, $m < 0$, the extrema in the buoyancy field lead the extrema in w by 90°. As a consequence, the buoyancy perturbations achieve their extremum along the dashed wave fronts. These dashed lines have been labeled "most buoyant" or "least buoyant" using (4.9). Now consider how the situation in Fig. 4.1 will evolve with time. According to (4.4), buoyancy per-

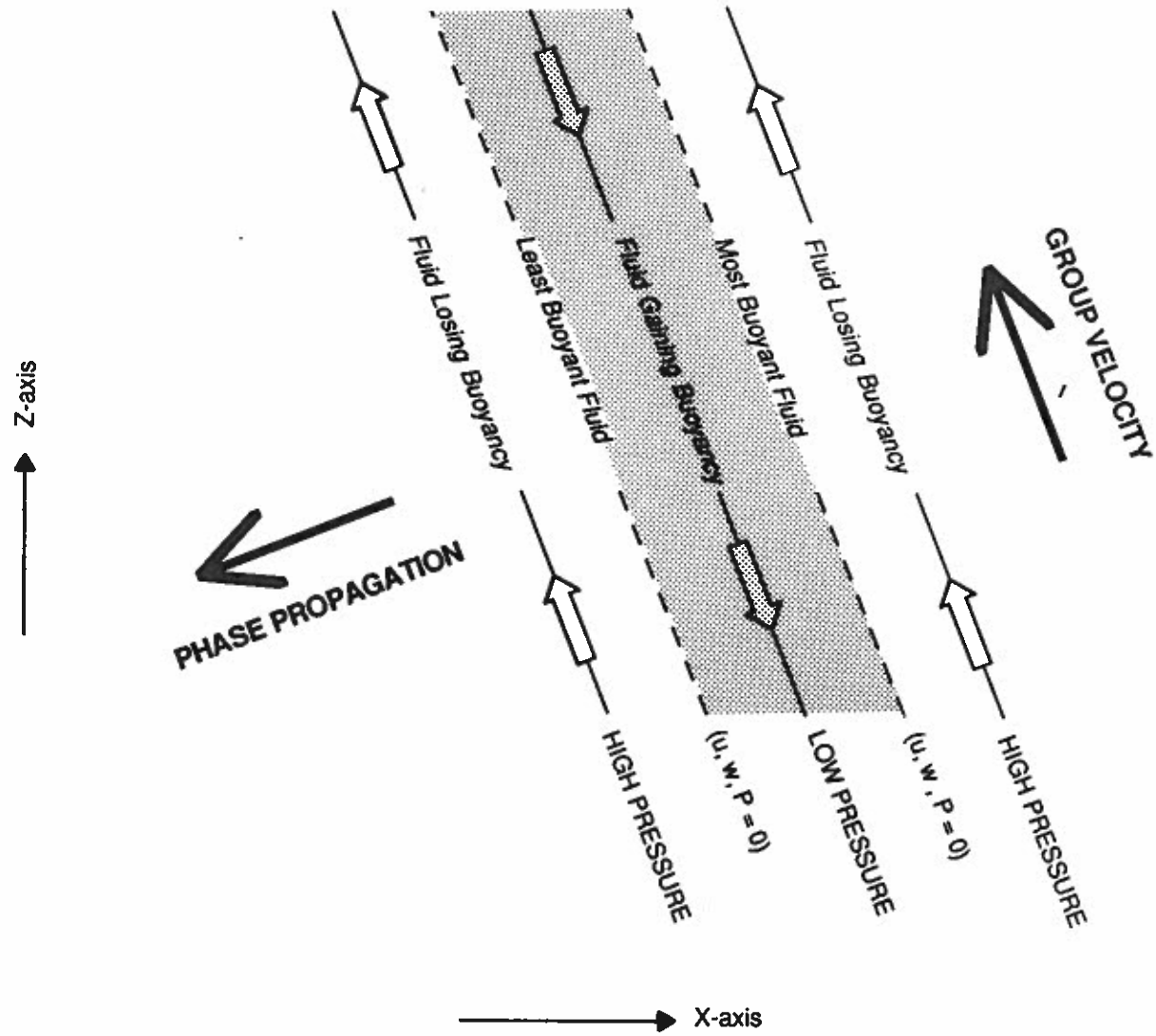

FIG. 4.1. The instantaneous distribution of velocity, pressure, and buoyancy perturbations in an internal gravity wave. This is a view in the x–z plane. The phase of the wave is constant along the slanting, dashed, and solid lines. Velocity and pressure perturbations have extrema along the solid lines; buoyancy perturbations are zero along the solid lines. Buoyancy perturbations have extrema, and velocity and pressure perturbations are zero along the dashed lines. Small arrows indicate the perturbation velocities, which are always parallel to the lines of constant phase. Large heavy arrows indicate the direction of phase propagation and the group velocity.

turbations develop through the action of vertical advection on the mean-state stratification. Since $w < 0$ everywhere within the shaded region in Fig. 4.1, the air within the shaded region is becoming more buoyant; therefore, the line of most buoyant fluid must be moving into the shaded region. Since the wave maintains itself as a coherent structure, the phase lines associated with the other perturbation quantities also propagate down and to the left, as indicated in Fig. 4.1. Note, for example, how the phase lines in the horizontal perturbation velocity field will shift in response to the horizontal pressure gradient. As evident in Fig. 4.1, *the lines of constant phase, or wave fronts, move perpendicular to the actual air-parcel trajectories.*

The total kinetic and potential energy (per unit mass) associated with the wave perturbations may be expressed as

$$E = \frac{1}{2}\left(u^2 + w^2 + \frac{b^2}{N^2}\right). \tag{4.12}$$

The governing equations (4.2)–(4.5) require that E satisfy

$$\frac{\partial E}{\partial t} + \frac{\partial Pu}{\partial x} + \frac{\partial Pw}{\partial z} = 0. \tag{4.13}$$

Thus, the waves transport energy in the direction of the energy flux vector $P\mathbf{V}$. Examination of the correlation

between P and $\mathbf{V}$ in Fig. 4.1 shows that energy is transported parallel to the air parcel trajectories and the wave fronts in the direction indicated by the "group velocity" vector. The group velocity, defined as $\mathbf{c}_g = (\partial\nu/\partial k, \partial\nu/\partial m)$, points in the direction of energy propagation because it satisfies the relation $\widehat{P\mathbf{V}} = \hat{E}\mathbf{c}_g$, where $\hat{\ }$ denotes an average over one wavelength. In summary, the preceding analysis of the structure of an internal gravity wave shows that *the phase speed is perpendicular to the energy flux (or group velocity) and the energy flux is directed parallel to the actual air parcel trajectories.*

4.3. Application to small-amplitude mountain waves

Several authors have provided thorough discussions of the linear theory of mountain waves in previous reviews or textbooks (Queney et al. 1960; Smith 1979; Gill 1982; Durran 1986b). Therefore, an extended exposition of linear mountain-wave theory will not be presented in the following section. Our focus will be on the application of the theory of section 4.2 to the basic case of a uniform airstream flowing over an infinite series of sinusoidal mountains. The generalization of this basic case to situations with more complex atmospheric structure and isolated topography will be summarized, but not discussed in detail.

4.3.1. Sinusoidal ridges; constant wind speed and stability

The most fundamental properties of small-amplitude mountain waves can be profitably examined by considering the steady-state, two-dimensional airflow over an infinite series of periodic ridges of the form

$$h(x) = h_m \cos kx. \tag{4.14}$$

The two-dimensional assumption is appropriate if the mountains extend indefinitely in the direction parallel to the ridge. As further simplifications, the Rossby number governing the flow (u_0k/f) is assumed large, so Coriolis accelerations may be neglected, and the atmosphere is assumed inviscid and Boussinesq. Then, if the mean horizontal wind speed u_0 is a constant, the dynamics of the problem are governed by equations identical to (4.2)–(4.5), except that each time derivative $\partial/\partial t$ is replaced by an advection term $u_0\partial/\partial x$. After two integrations with respect to x (the integration constants are zero because w has no mean or linear trend), the equation corresponding to (4.6) reduces to

$$\frac{\partial^2 w}{\partial x^2} + \frac{\partial^2 w}{\partial z^2} + \frac{N^2}{u_0^2} w = 0. \tag{4.15}$$

Solutions to (4.15) may be written in the form

$$w = \Re\{Ae^{i(kx+mz)} + Be^{i(kx-mz)}\}, \tag{4.16}$$

where $\Re$ denotes the real part, A and B are complex coefficients, and

$$m = (N^2/u_0^2 - k^2)^{1/2}. \tag{4.17}$$

In (4.16), redundant solutions are eliminated by choosing the positive root for m and requiring $k > 0$.

The coefficients A and B are determined by the boundary conditions. At the lower boundary, the velocity normal to the topography must vanish. This condition can be approximated, to the same order of accuracy as the linearized equations, by

$$w(x, 0) = u_0 \frac{\partial h}{\partial x} = -u_0 k h_m \sin kx. \tag{4.18}$$

Substitution of (4.16) into (4.18) yields the conditions

$$\Re\{A\} + \Re\{B\} = 0; \quad \Im\{A\} + \Im\{B\} = u_0 h_m k, \tag{4.19}$$

where $\Im$ denotes the imaginary part. A second boundary condition is imposed as $z \to \infty$. The nature of this boundary condition depends on the vertical structure of the solution, which depends on the relative magnitudes of u_0k and N. When $u_0k > N$, the solution (4.16) may be written

$$w = \Re\{Ae^{-\mu z}e^{ikx} + Be^{\mu z}e^{ikx}\}, \tag{4.20}$$

where, according to (4.17), μ is a real number equal to $(k^2 - N^2/u_0^2)^{1/2}$. In this Boussinesq system, it is physically unreasonable for the wave amplitude to grow exponentially without bound as $z \to \infty$, so the upper boundary condition requires that $B = 0$. Then from (4.19), $\Re\{A\} = 0$ and $\Im\{A\} = u_0h_mk$; the complete solution appears in (4.23).

Now consider the case where $u_0k < N$, then m is real and both A and B are coefficients of waves that are bounded as $z \to \infty$. Instead of a simple condition on the boundedness of the solution, the appropriate upper boundary condition for this linear steady-state problem is the "radiation condition," which requires that all waves at an arbitrarily great height above the mountain must be transporting energy away from the mountain. In general, the imposition of a radiation boundary condition as $z \to \infty$ is justified whenever all processes that could generate waves (such as nonlinear wave–wave interactions or reflections from regions where there is a rapid change in atmospheric structure) are contained within some finite height of the topography. In order to impose the radiation condition, it is necessary to determine the direction of the energy transport by each wave in (4.16). One approach, due to Eliassen and Palm (1960), is to determine the vertical energy flux $\widehat{Pw}$. The perturbation pressure associated with each wave may be evaluated from the horizontal momentum equation, the continuity equation,

and (4.16). In the wave with coefficient A (the upstream tilting wave, whose vertical velocity will be denoted w_a),

$$P_a = \frac{u_0 m}{k} \Re\{Ae^{i(kx+mz)}\}. \tag{4.21}$$

In the downstream tilting wave

$$P_b = -\frac{u_0 m}{k} \Re\{Be^{i(kx-mz)}\}. \tag{4.22}$$

It follows that $\widehat{P_a w_a} > 0$, so the upstream tilting wave is associated with upward energy flux. Similarly, $\widehat{P_b w_b} < 0$, and the downstream tilting wave is associated with downward energy flux. The radiation boundary condition is thus imposed by requiring $B = 0$. Then using (4.19), $\Re\{A\} = 0$ and $\Im\{A\} = u_0 h_m k$.

In summary, the perturbation vertical velocity field in waves forced by the sinusoidal terrain profile (4.14) can be written

$$w(x, z) = \begin{cases} -u_0 h_m k e^{-\mu z} \sin kx, & u_0 k > N; \\ -u_0 h_m k \sin(kx + mz), & u_0 k < N. \end{cases} \tag{4.23}$$

The difference between these two wave structures is illustrated in Fig. 4.2. In the case $u_0 k > N$ (Fig. 4.2a), the waves decay exponentially with height (evanescent waves) and the wave crests are aligned vertically. In the case $u_0 k < N$ (Fig. 4.2b), the waves propagate vertically without loss of amplitude and the wave crests tilt upstream with height. The waves decay away from the forcing when the intrinsic frequency exceeds the Brunt–Väisälä frequency ($u_0 k > N$) because, as discussed in section 4.2, there is no way for buoyancy restoring forces to support the oscillation. On the other hand, when the intrinsic frequency is less than the Brunt–Väisälä frequency, vertical propagation occurs because buoyancy restoring forces can support air-parcel oscillations along a path slanted off the vertical at an angle $\phi = \cos^{-1}(u_0 k/N)$. In steady mountain waves ϕ is the angle at which lines of constant phase tilt off the vertical (see the dashed line in Fig. 4.2b). A schematic diagram of the perturbation velocity, pressure, and density fields in Fig. 4.2b would be identical to that in Fig. 4.1. However, since there is a mean flow in the mountain-wave problem, the actual air-parcel trajectories do not follow the slanted paths in Fig. 4.1, but rather the wavy lines shown in Fig. 4.2.

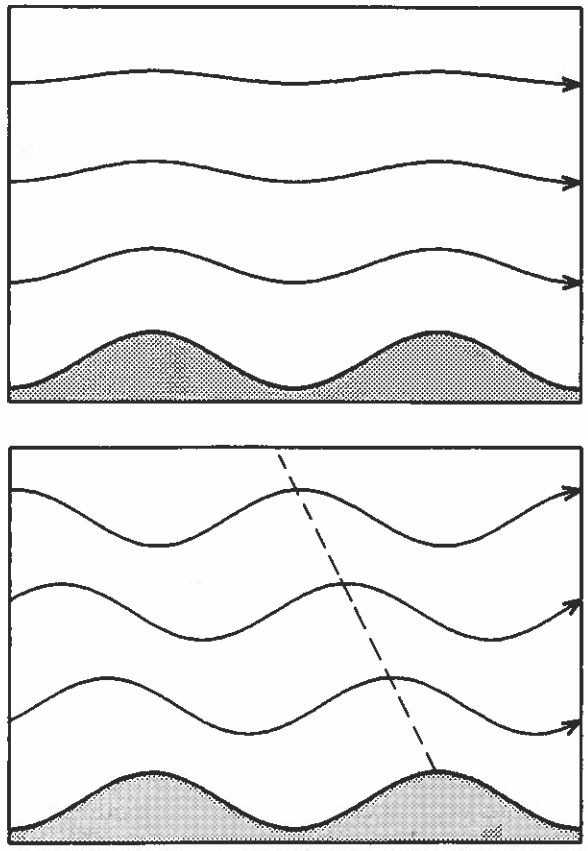

FIG. 4.2. Streamlines in steady airflow over an infinite series of sinusoidal ridges when (a) $u_0 k > N$, or (b) $u_0 k < N$. The dashed line (b) shows the upstream tilt of the lines of constant phase. Unless otherwise stated, the airflow in this and all subsequent figures is from left to right.

4.3.2. *Isolated mountain; constant wind speed and stability*

The mountain-wave solution (4.23) applies only to an airstream with constant basic-state wind speed and stability flowing across an endless series of sinusoidal ridges. If more realistic terrain profiles and atmospheric structures are considered, other linear solutions can be obtained that strongly resemble observed mountain waves. In the remainder of this section, we will describe how the wave response is influenced by isolated topography and vertical variations in atmospheric wind speed and stability. In order to focus on the physical results, the mathematical derivations will be omitted; they can be found in Smith (1979) or Queney et al. (1960).

Suppose that the mountain contour consists of a single ridge, so that the terrain elevation drops to some reference level at all distances sufficiently far upstream and downstream. Just as Fourier series can be used to represent a wide variety of periodic functions with an infinite sum of sines and cosines, the isolated mountain can generally be constructed from periodic functions by the use of Fourier transforms. The Fourier transform (F) of a real function ϕ and its inverse (F^{-1}) may be defined:

$$\begin{aligned} \tilde{\phi}(k) &= F[\phi(x)] = \frac{1}{\pi} \int_{-\infty}^{\infty} \phi(x) e^{-ikx} dx, \\ \phi(x) &= F^{-1}[\tilde{\phi}(k)] = \Re \int_0^{\infty} \tilde{\phi}(k) e^{ikx} dk. \end{aligned} \tag{4.24}$$

The Fourier transform is particularly useful in this application because it has the property that $F(\partial^n\phi/\partial x^n) = (ik)^n\tilde{\phi}$.

When N and u_0 are constant, each component of the Fourier transformed vertical velocity $\tilde{w}(k, z)$ must satisfy the Fourier transform of the governing equation (4.15),

$$\frac{\partial^2\tilde{w}}{\partial z^2} + \left(\frac{N^2}{u_0^2} - k^2\right)\tilde{w} = 0. \tag{4.25}$$

The solution to (4.25), subject to appropriate upper and lower boundary conditions, is

$$\tilde{w}(k, z) = iku_0\tilde{h}(k)\exp[i(N^2/u_0^2 - k^2)^{1/2}z], \quad k > 0. \tag{4.26}$$

Equation (4.26) is just the complex analog of (4.23); therefore, each component $\tilde{w}(k, z)$ of the transformed vertical velocity is identical to the velocity forced by an infinite series of sinusoidal ridges having wavenumber k and amplitude $\tilde{h}(k)$. Thus, the solutions obtained in section 4.3.1. are also applicable to the case of isolated topography. The only complication arises from the requirement that after $\tilde{w}(k, z)$ is determined, the total vertical velocity $w(x, z)$ must be obtained by computing an inverse Fourier transform. According to (4.26), the relative weight attached to each individual wavenumber in the composite solution is determined by Fourier transform of the terrain profile.

Queney (1948) calculated solutions for the waves generated in a fluid, with constant N and u_0, flowing over the "Witch of Agnesi" terrain profile:

$$h(x) = \frac{h_m a^2}{a^2 + x^2}, \tag{4.27}$$

where h_m is the maximum mountain height and a determines the mountain width. For a very narrow mountain, $u_0a^{-1} \gg N$; the profile is dominated by wavenumbers greater than N/u_0, and the mountain primarily forces evanescent waves (Fig. 4.3a; cf. Fig. 4.2a). For a wide mountain, $u_0a^{-1} \ll N$; the dominant wavenumbers are less than N/u_0, and the waves propagate vertically with lines of constant phase tilting upstream (Fig. 4.3b; cf. Fig. 4.2b). The wide mountain limit, being equivalent to the hydrostatic limit, eliminates the dependence of vertical structure on the horizontal wavenumber in (4.26). As a result, the mountain profile is reproduced at every level that is an integral multiple of $2\pi u_0/N$. This result is independent of the shape of the mountain contour. It should be emphasized that if an isolated mountain is sufficiently wide that it only forces hydrostatic waves (but not so wide that Coriolis forces become important), there will only be one wave crest in the air flowing over the mountain. Additional crests do not appear downstream from the mountain unless nonhydrostatic effects are significant. The most obvious way that nonhydrostatic effects manifest themselves is in the development of trapped lee waves.

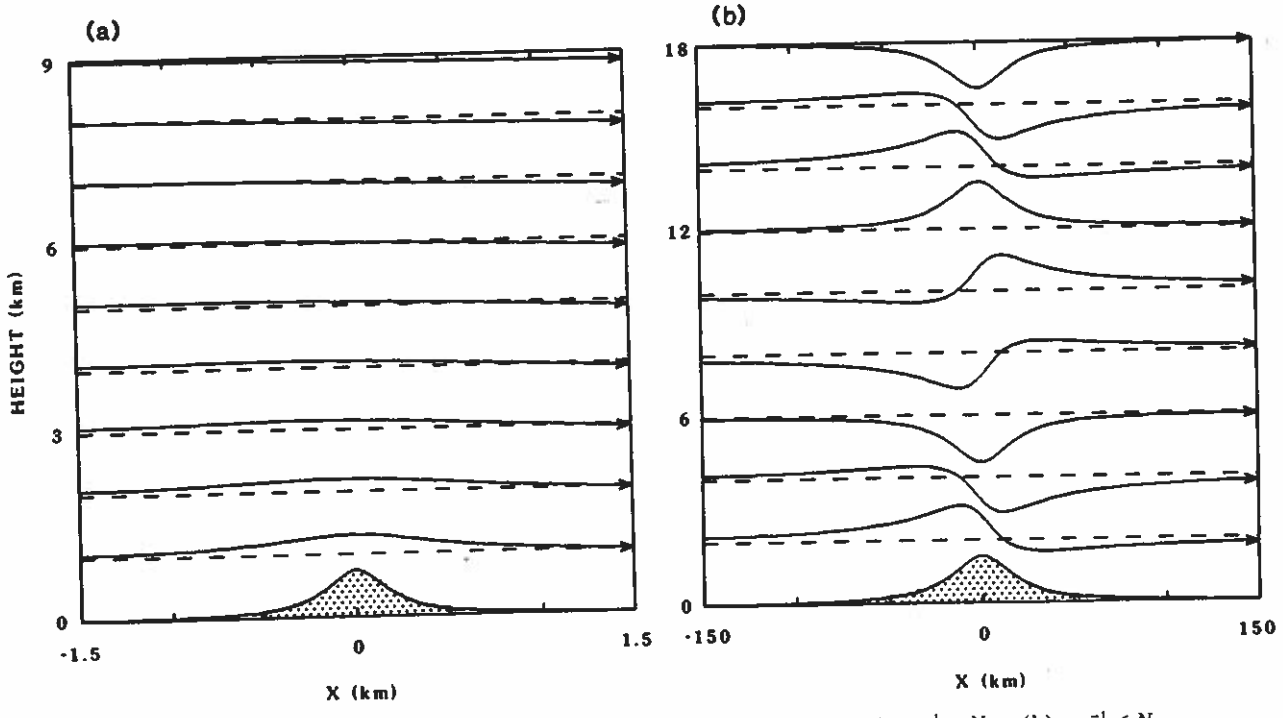

FIG. 4.3. Streamlines in steady airflow over an isolated bell-shaped ridge when (a) $u_0a^{-1} \gg N$, or (b) $u_0a^{-1} \ll N$.

4.3.3. Vertical variations in wind speed and stability

Now consider the effects of vertical variations in the mean atmospheric structure. The most important variations are those that occur in u_0 and N. Vertical variations in u_0 and N can support a new qualitatively different type of wave—the trapped lee wave. The airflow in a series of trapped lee waves (also known as resonant lee waves) is shown in Fig. 4.4; most of the wave activity is confined to the lower troposphere on the lee side of the mountain. Scorer (1949) used linear theory to show that trapped waves arise as a result of vertical variations in $N(z)$ and $u_0(z)$. These variations introduce an additional term in the governing equation, so that (4.15) becomes

$$\frac{\partial^2 w}{\partial x^2} + \frac{\partial^2 w}{\partial z^2} + l^2 w = 0, \tag{4.28}$$

where l is the Scorer parameter, defined as

$$l^2 = \frac{N^2}{u_0^2} - \frac{1}{u_0}\frac{d^2 u_0}{dz^2}. \tag{4.29}$$

Scorer considered the case where l was constant within each of two layers. (Note that a discontinuity in l does not require a discontinuity in either θ_0 or u_0.) Scorer showed that a necessary condition for the existence of trapped waves in the two-layer problem is that

$$l_L^2 - l_U^2 > \frac{\pi^2}{4H^2}. \tag{4.30}$$

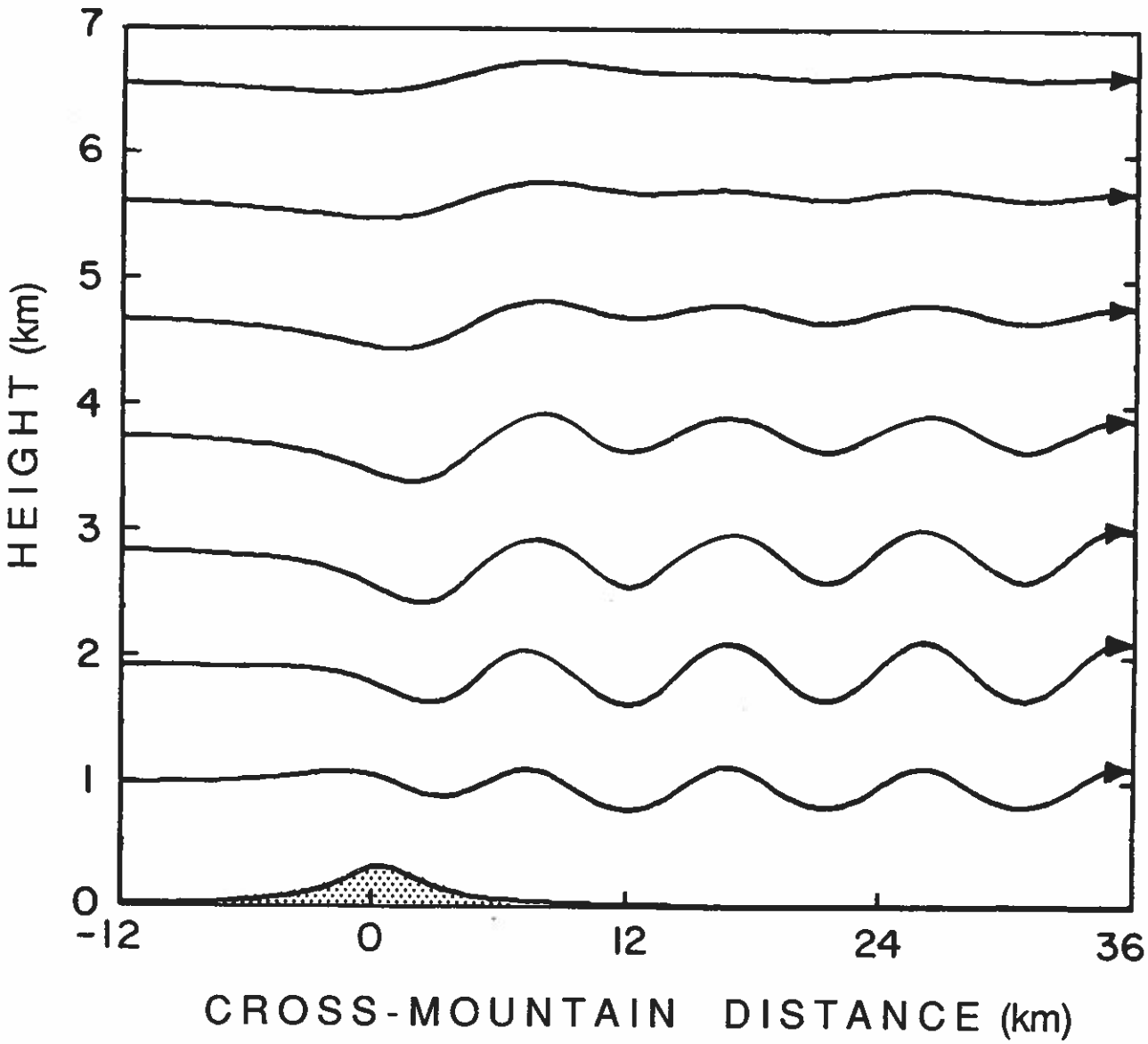

FIG. 4.4. Streamlines in steady airflow over an isolated ridge when the vertical variation in the Scorer parameter permits trapped waves.

In the preceding paragraphs, l_U and l_L are the Scorer parameters in the upper and lower layers, and H is the depth of the lower layer. As implied in Eq. (4.30), the difference in wave propagation characteristics in the two layers must exceed a certain threshold before the waves can be "trapped."

Earlier in this section it was emphasized that vertically propagating waves are permitted when $u_0 k < N$. The appropriate generalization of this result to an environment with vertical wind shear is the condition that $k < l$. The horizontal wavenumber of any resonant lee wave in the two-layer system satisfies $l_L > k > l_U$, implying that the wave propagates vertically in the lower layer and decays exponentially with height in the upper layer. As shown in Fig. 4.4, trapped waves have no tilt, even though they can propagate vertically in the lower layer. The reason for this is that wave energy is repeatedly reflected, without loss of amplitude, from the upper layer and the flat ground downstream from the mountain. As a result, the downstream disturbance is the superposition of equal-amplitude upward and downward propagating waves, a combination that has no tilt.

Vertical variations in l not only provide a way of supporting trapped waves, they can also modify the amplitude of long-wavelength hydrostatic waves that propagate vertically through both layers. The influence of rapid changes in l on vertically propagating waves will be discussed in the following section on downslope windstorms.

4.4. Downslope windstorms

Every few years the eastern slope of the Colorado Front Range (part of the Rocky Mountains) experiences a damaging windstorm, with peak gusts as high as 60 m s^{-1}. These storms have received considerable attention in the atmospheric science community due, in part, to the high concentration of meteorologists living in Boulder, Colorado who are exposed to the storms. Similar winds are also observed along the lee slopes of many other mountain barriers. The local names for these winds include the Alpine foehn, the Rocky Mountain chinook, the Yugoslavian bora, and the Argentine zonda. Over the last ten years there has been considerable debate over the relative merits of three different mechanisms that had been proposed to account for the development of strong downslope winds. Recently, evidence has begun to accumulate supporting the idea that there is a fundamental dynamical analog between the flow of water over an obstacle in a hydraulic jump and flow of air over a ridge in a downslope windstorm. In this section we will examine the three mechanisms that have been proposed to explain the downslope wind phenomena, and the recent work that appears to support the hydraulic analog.

4.4.1. *Three explanations for the production of severe downslope winds*

The oldest of the three conceptual models was proposed by Long (1953a) over 35 years ago. Long suggested that there is a fundamental similarity between downslope windstorms and hydraulic jumps—essentially the same theory that is currently enjoying a resurgence in popularity. In order to better understand Long's hypothesis, let us consider the dynamics of a homogeneous fluid flowing over a ridgelike obstacle. Assume that the flow is in hydrostatic balance and bounded by a free surface. Then, if there are no variations in the coordinate direction parallel to the ridge axis, the steady-state behavior of the system is governed by the shallow-water momentum and continuity equations:

$$u\frac{\partial u}{\partial x} + g\frac{\partial D}{\partial x} + g\frac{\partial h}{\partial x} = 0, \tag{4.31}$$

$$\frac{\partial uD}{\partial x} = 0. \tag{4.32}$$

Here x is the coordinate direction oriented perpendicular to the ridgeline, u is the velocity in the x direction, D is the thickness of the fluid, and h is the height of the obstacle. Using (4.32) to substitute for $\partial u/\partial x$ in (4.31), one obtains:

$$(1 - \mathrm{Fr}^{-2})\frac{\partial (D + h)}{\partial x} = \frac{\partial h}{\partial x}, \tag{4.33}$$

where the Froude number Fr, defined as

$$\mathrm{Fr}^2 = \frac{u^2}{gD}, \tag{4.34}$$

is the ratio of the fluid velocity to the speed of propagation of linear shallow-water gravity waves. According to (4.33), the free surface can either rise or fall as the fluid encounters rising bottom topography, depending on the magnitude of Fr. The case Fr $>$ 1 (supercritical flow) is shown in Fig. 4.5a; the fluid thickens and slows down as it crosses the top of the obstacle, reaching its minimum speed at the crest. The accelerations experienced by the fluid are qualitatively similar to those experienced by a hockey puck traversing a frictionless mound of ice. The case Fr $<$ 1 (subcritical flow) shown in Fig. 4.5b seems counterintuitive in that the fluid thins and accelerates as it crosses the top of the obstacle, reaching its maximum speed at the crest.

Why does the fluid accelerate as it encounters rising topography in Fig. 4.5b? Why does the dependence on Fr appear in (4.33)? The steady-state momentum equation (4.31) requires a three-way balance between nonlinear advection (the first term), pressure gradient forces arising from changes in the fluid depth (the second term), and

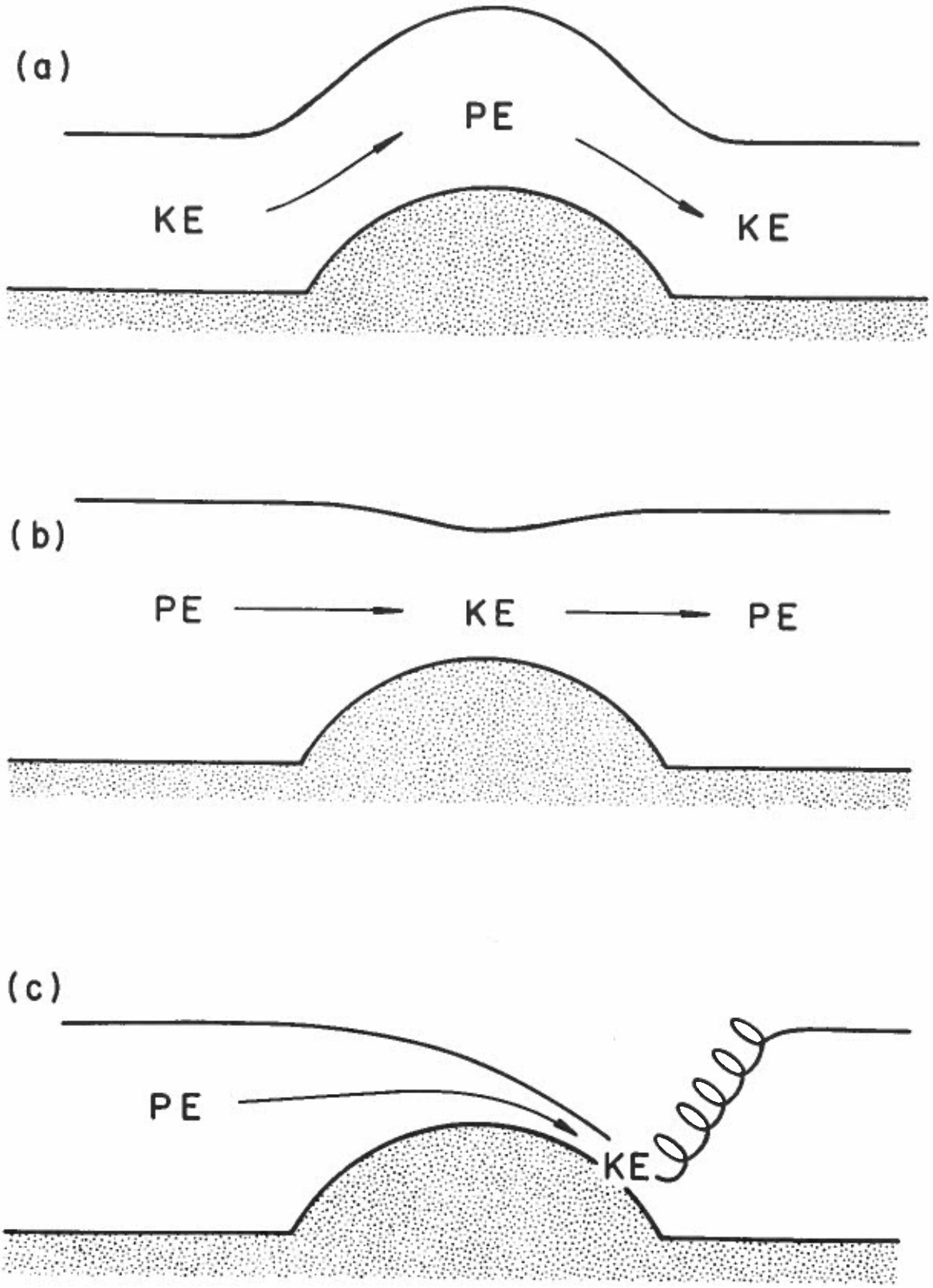

FIG. 4.5. Behavior of shallow water flowing over an obstacle: (a) everywhere supercritical flow, (b) everywhere subcritical flow, (c) hydraulic jump.

work done per unit horizontal displacement moving against gravity along the sloping topography (the third term). Using (4.32) one can show that

$$\left(u\frac{\partial u}{\partial x}\right)\Big/\left(g\frac{\partial D}{\partial x}\right)=\left(u\frac{\partial u}{\partial x}\right)\Big/\left(\frac{-gD}{u}\frac{\partial u}{\partial x}\right)=-\mathrm{Fr}^2. \tag{4.35}$$

Thus, advection always opposes the pressure gradient due to changes in fluid depth. Furthermore, *Fr^2 is the ratio of the magnitude of nonlinear advection to the magnitude of the pressure gradient generated by changes in the fluid depth.* In supercritical flow (Fr > 1) nonlinear advection dominates the pressure gradient term and the three-way balance in (4.31) is satisfied when fluid parcels are accelerated in the same direction as the gravitational force. Consequently, as a fluid parcel ascends the obstacle, it slows, converting kinetic energy (KE) to potential energy (PE); after passing the crest, it reaccelerates as PE is converted back to KE (Fig. 4.5a). On the other hand, in subcritical flow (Fr < 1) the pressure gradient term dominates advection and (4.31) is balanced when fluid parcels accelerate in the direction opposite the gravitational force. Then, as shown in Fig. 4.5b, a fluid parcel ascending the obstacle accelerates as the free surface drops and PE is converted to KE; after passing the crest it decelerates as KE is converted back to PE. The disturbance centered over the obstacle in Fig. 4.5b is a stationary surface gravity wave.

The flow regime that Long proposed as a model for downslope windstorms is shown in Fig. 4.5c. If there is a sufficient acceleration in the stationary gravity wave; i.e., a sufficient increase in velocity and decrease in thickness as the fluid ascends toward the crest, a transition from subcritical to supercritical flow occurs at the top of the obstacle (Fig. 4.5c). Since the flow along the lee slope is supercritical, the fluid continues to accelerate as it falls down the mountain; it eventually recovers to the ambient downstream conditions in a turbulent hydraulic jump. Very high velocities are produced along the lee slope because PE is converted to KE during the entire time that a fluid parcel traverses the mountain. The deceleration that would otherwise occur in the lee-side portion of the gravity wave is disrupted when the flow becomes supercritical. Further discussion of the hydraulic model may be found in Long (1954) and Houghton and Kasahara (1968).

One uncertainty associated with the application of the hydraulic model to the atmosphere is that the atmosphere is not bounded by a free surface. The presence of a free surface (or in different formulations, a rigid lid) prevents energy transport through the upper boundary of the hydraulic layer; however, internal gravity waves can transport energy vertically to great heights in the unbounded continuously stratified atmosphere. In at least some instances, it appears that this energy can be removed in the upper atmosphere without significantly affecting the low-level wave structure. Thus, the hydraulic model may be too limited for application to the atmosphere. Furthermore, as indicated by the variation in spacing between streamlines in Figs. 4.2b and 4.3b, the surface wind speed distribution in vertically propagating internal gravity waves is asymmetric about the crest, with a maximum along the lee slope. The preceding observations suggest an alternative to hydraulic theory, which better accounts for the possibility of vertical energy transport, namely that downslope windstorms are produced by large-amplitude vertically propagating mountain waves. Eliassen and Palm (1960) showed that when an upward propagating linear gravity wave encounters a region in which the Scorer parameter changes rapidly, part of its energy can be reflected back into a downward propagating wave. Klemp and Lilly (1975) extended the results of Eliassen and Palm, and Blumen (1965), to the case of small-amplitude hydrostatic waves in a multilayer atmosphere with constant stability and wind shear in each layer. Klemp and Lilly suggested downslope windstorms occur when the atmosphere is tuned so that the partial reflections at each interface produce an optimal superposition of upward and downward propagating waves. They found that, in practice, the most important tuning requirement is that the tropopause be located one-half vertical wavelength above the ground.

The third explanation for the development of strong downslope winds was proposed on the basis of simulations performed with a comprehensive numerical model. In a series of papers Clark and Peltier (1977, 1984), Peltier and Clark (1979, 1983), and Clark and Farley (1984) found significant increases in the lee-slope surface winds occurred after vertically propagating waves became statically unstable and "broke." The wave-breaking region was characterized by strong mixing and a local reversal of the cross-mountain flow. They proposed that this "wave-induced critical layer" acts as a boundary, reflecting upward propagating waves back toward the mountain. The terminology "wave-induced critical layer" derives from the idea that the wave overturning region influences the underlying flow in a manner similar to a turbulent (i.e., low Richardson number[1]) mean-state critical layer. A critical layer (or critical level) occurs where the phase speed of the wave is equal to the mean flow velocity. In the case of stationary mountain waves, a critical level occurs where the mean flow is zero. If the Richardson number at the critical layer is less than $\frac{1}{4}$, nonlinear waves encountering a critical layer are believed to reflect from

[1] The Richardson number, $\mathrm{Ri} = N^2/(U_z)^2$, is a measure of the ratio of the buoyancy restoring force to the shear.

that layer without significant loss in amplitude. Using linear theory to describe the reflection process, Peltier and Clark suggested that if the depth of the cavity between the self-induced critical layer and the mountain is suitably tuned, the reflections at the critical layer should produce a resonant wave that amplifies linearly with time and ultimately produces very strong surface winds. Additional numerical studies by many different researchers have repeatedly verified the importance of wave breaking in the development of strong surface winds in both the 11 January 1972 Boulder windstorm and in cases with constant upstream values of N and u_0.

4.4.2. *A comparison of the hydraulic and the vertically propagating wave theories*

The linear theory of vertically propagating waves predicts that some enhancement of the lee-side surface winds will be produced by arbitrarily small mountains and that the strength of the horizontal wind perturbation will scale linearly with the height of the mountain. In contrast, hydraulic theory suggests that strong downslope winds will only occur if the mountain height exceeds the threshold required to force a transition to supercritical flow. This fundamental difference in amplitude dependence can be used to test each theory. Consider first the simple case when the upstream profiles of u_0 and N are constant with height. Then, within the accuracy of the Boussinesq approximation, the finite-amplitude response can be calculated analytically from Long's equation (Long 1953b). As shown by Lilly and Klemp (1979), these finite-amplitude solutions are both qualitatively and quantitatively similar to the solutions obtained from linear theory. Thus, on the basis of the constant N and u_0 case, one might suppose that linear theory provides a satisfactory description of finite-amplitude mountain waves. However, as noted by Smith (1977), the assumption of constant u_0 and N places a special constraint on the nonlinear interactions possible in steady flow, and caution should be exercised in generalizing from the constant u_0 and N case to more realistic atmospheric profiles.

A slightly more complex atmospheric structure was studied by Durran (1986a), who used a numerical model to examine the effects of nonlinearity on the partial reflection of vertically propagating mountain waves in a mean state with constant wind speed and a two-layer stability structure where the Brunt–Väisälä frequency was constant within each layer. In each case, a measure of the amplitude of the wave response was obtained by calculating the pressure drag exerted on the mountain by the flow

$$\int_{-\infty}^{\infty} p \frac{\partial h}{\partial x} dx. \tag{4.36}$$

The drag was normalized by $\pi \rho N_L u_0 h_m^2/4$, the drag produced by linear hydrostatic waves on a Witch of Agnesi mountain [see Eq. (4.27)] in a single-layer atmosphere with constant wind speed and stability equal to that in the lowest layer. This normalization emphasizes the effects of atmospheric structure and nonlinearity on the drag. According to the linear theory of hydrostatic mountain waves, when the thickness of the lower layer is one-half vertical wavelength ($\pi u_0/N_L$), the normalized drag (D_n) is N_U/N_L. When the thickness of the lower layer is one-quarter vertical wavelength, the effect of the layering reverses and $D_n = N_L/N_U$.

Durran considered the four basic configurations shown in Fig. 4.6. In Figs. 4.6a,b the more stable layer ($N = 0.02$ s^{-1}) is on the bottom; in Figs. 4.6c,d the less stable layer ($N = 0.01$ s^{-1}) is on the bottom; in all cases $u_0 = 20$ m s^{-1}. The depth of the lowest layer is set to one-quarter or one-half vertical wavelength, so that linear theory predicts values for D_n of 2.0 in the cases in panels 4.6a,d and 0.5 for those in panels 4.6b,c. Numerical simulations conducted with a maximum value of $Nh_m/u_0 = 0.001$ confirmed that the model was capable of reproducing the linear result in circumstances where nonlinear effects are genuinely insignificant. When $(Nh_m/u_0)_{\max}$ was increased to 0.6, nonlinear processes had a significant influence on the solution. The amplification predicted in the linear limit in panels 4.6a,d disappeared in the finite-amplitude simulations as D_n dropped to values less than or equal to 1. The most dramatic differences between linear theory and the finite-amplitude simulations appeared in Fig. 4.6b, where D_n increased from a linear value of 0.5 to a nonlinear value of 2.9. Although there are quantitative differences, the waves in Figs. 4.6a,c,d are qualitatively similar to the vertically propagating waves described by linear theory. On the other hand, the situation in panel 4.6b is very different: it is the only finite-amplitude case associated with high drag (and high surface winds) and the lower-layer flow qualitatively resembles a hydraulic jump.

A detailed look at the effects of nonlinearity on the drag and surface wind speed in a two-layer atmosphere similar to that shown in Fig. 4.6b is provided in Fig. 4.7. The normalized drag D_n is relatively independent of mountain height for $N_L h_m/u_0 < 0.2$ and $N_L h_m/u_0 > 0.6$. In between these two limits, there is a rapid transition between low and high drag regimes. Linear theory predicts that the mountain drag should vary as h_m^2, and this amplitude dependence is removed when the drag is normalized. Thus, the variation of D_n with $N_L h_m/u_0$ is due exclusively to nonlinear effects. The amplitude dependence revealed in Fig. 4.7 is qualitatively similar to the increase in drag that occurs in hydraulic theory as the height of the obstacle becomes sufficient to force a transition from subcritical to supercritical flow. The finite-amplitude results shown

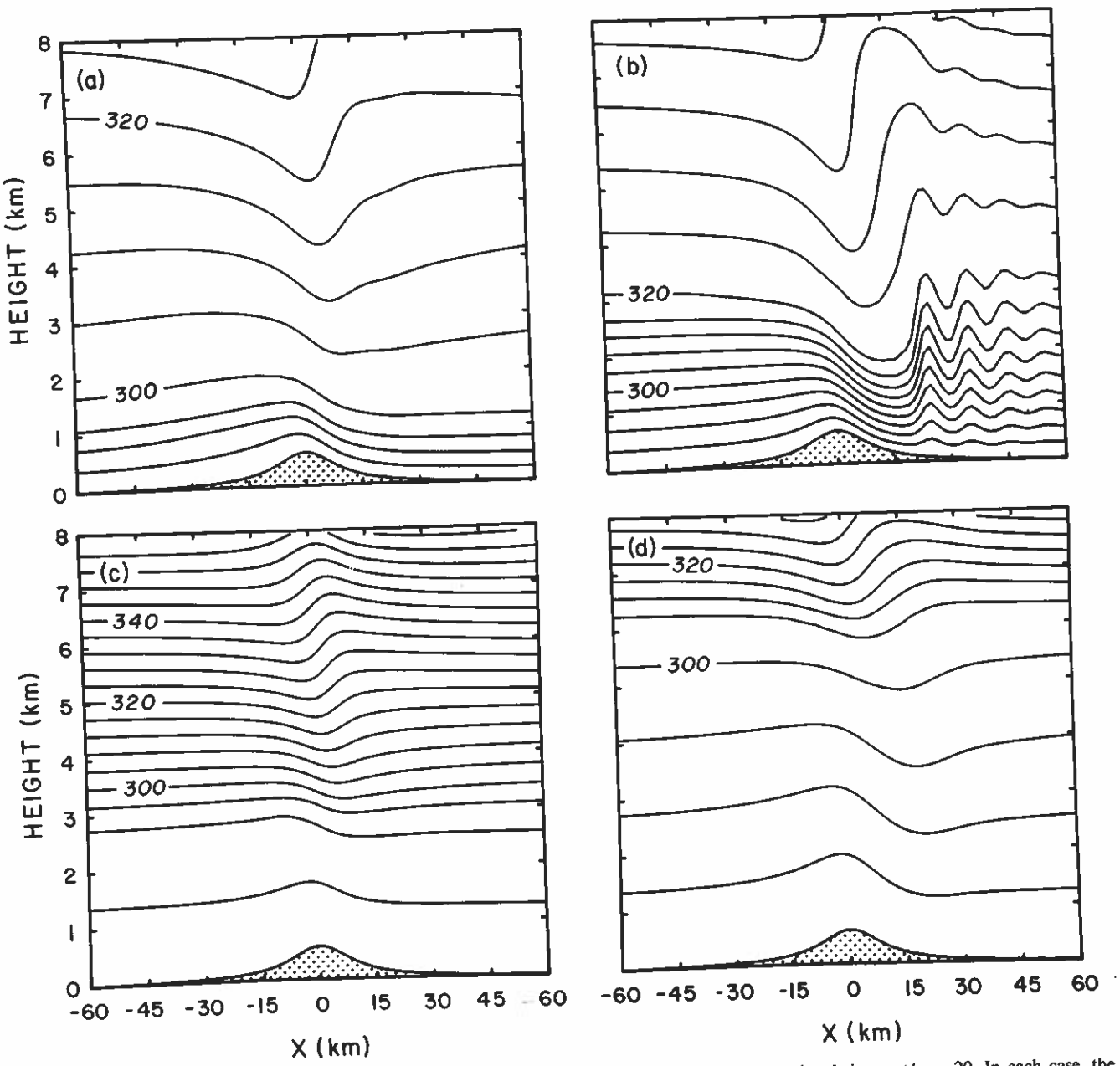

FIG. 4.6. Isentropes in a two-layer atmosphere flowing over an isolated mountain at a nondimensional time $u_0 t/a = 20$. In each case, the maximum value of Nh_m/u_0 is 0.6. (a) interface at $\frac{1}{4}$ vertical wavelength, $N_L = 2N_U$; (b) interface at $\frac{1}{2}$ wavelength, $N_L = 2N_U$; (c) interface at $\frac{1}{4}$ wavelength, $N_L = \frac{1}{2}N_U$; (d) interface at $\frac{1}{2}$ wavelength, $N_L = \frac{1}{2}N_U$. (From Durran 1986a.)

in Fig. 4.7 deviate significantly from linear theory, even when the mountain is very small. For example, when $N_L h_m/u_0 = 0.3$, D_n is more than double its true linear value; however, as shown by Lilly and Klemp (1979), if N and u_0 were everywhere constant and Nh_m/u_0 was 0.3, there would be very little quantitative difference between the linear drag and the drag in the finite-amplitude solution. Thus, the sensitivity of the solution to nonlinear processes is greatly enhanced by the presence of the interface.

Further similarities between the two-layer solutions and hydraulic theory are shown in Fig. 4.8, in which the mountain height is fixed and the depth of the lowest, most stable layer is varied. As the depth of the lower layer increases, the flow in the lower layer first assumes a form similar to everywhere supercritical flow (Fig. 4.8a), then it resembles a propagating jump (Fig. 4.8b), a stationary jump (Fig. 4.8c), and finally, everywhere subcritical flow (Fig. 4.8d). The same dependence of the flow on fluid depth is observed in hydraulic theory (Houghton and Ka-

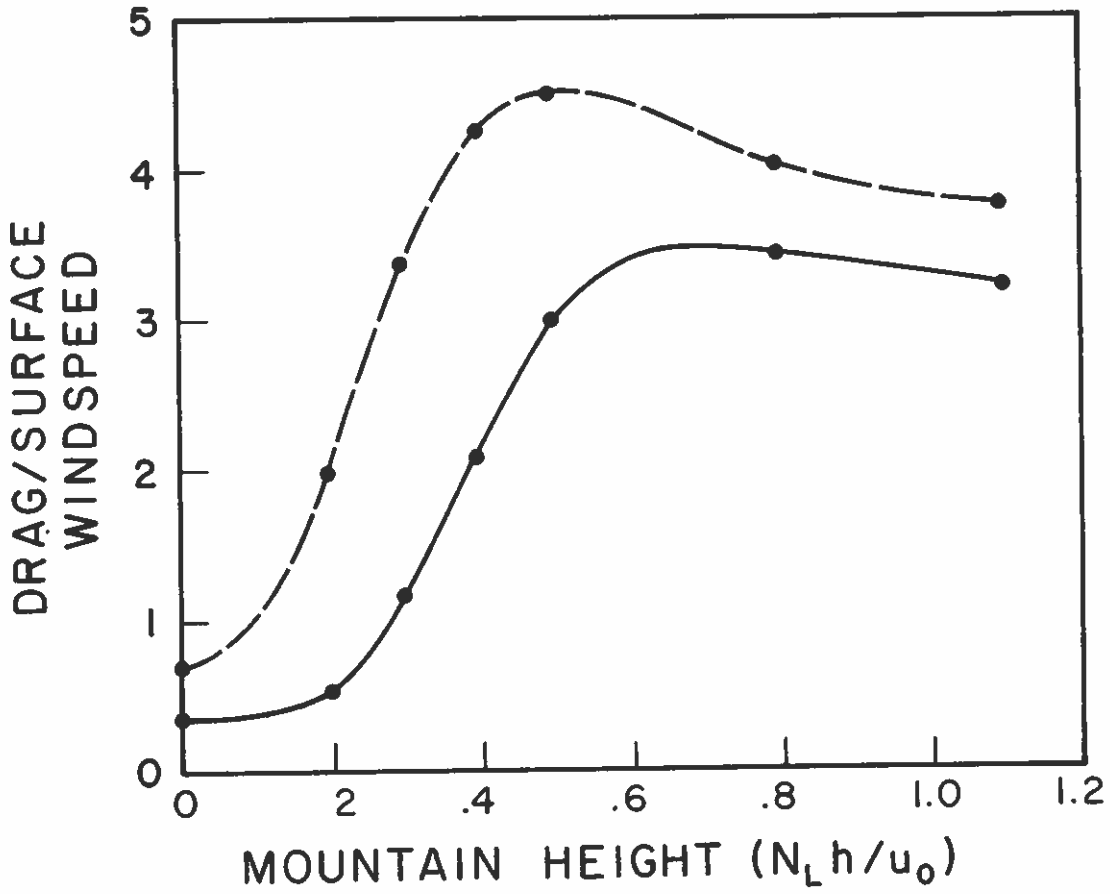

FIG. 4.7. Pressure drag (solid) and maximum surface wind speed perturbation (dashed) as a function of nondimensional mountain height $N_L h_m/u_0$ for a two-layer atmosphere with $N_L = 2.5N_U$. The drag is normalized by $\pi\rho N u_0 h_m^2/4$ and the wind speed by $Nh_m/2$ where ρ, u_0, and N are evaluated at the surface. (From Durran 1986a.)

sahara 1968). In summary, Durran's (1986a) results suggest that the partial reflection of vertically propagating waves from a layer interface is strongly dependent on wave amplitude. Furthermore, in those cases associated with high surface wind speeds and high drags, the influence of the interface on the nonlinear solution is qualitatively similar to that of a free surface in hydraulic theory.

4.4.3. A comparison of the hydraulic and the wave-breaking mechanisms

Evidence from observations (Smith 1987) and numerical models (Clark and Peltier 1977, and many others) suggests that wave breaking plays an important role in many downslope windstorms. Clark and Peltier (1977) suggested that after the isentropes in a mountain wave overturn, a resonant cavity forms between the terrain and the wave-breaking region, and the wave within that cavity amplifies dramatically. Peltier and Clark's (1983) mathematical model of wave amplification in this resonant cavity is based on linear theory and the physical assumption that the wave-overturning region behaves like a critical level where the Richardson number is less than $\frac{1}{4}$. Smith (1985a), and Smith and Sun (1987), have offered another mathematical model of the wave-breaking amplification process, beginning with the same fundamental assumption used by Clark and Peltier: that the breaking region imposes an effective upper boundary condition that traps energy within the underlying flow. Smith's mathematical treatment of the upper boundary is based on the identification of a hypothetical "dividing streamline" separating the laminar flow beneath the wave-breaking region from the turbulent flow above. Smith obtained an upper boundary condition stating that the cross-mountain wind speed is constant along the dividing streamline, by postulating that 1) the turbulent flow in the breaking region is well mixed, and 2) pressure perturbations at the top of the well-mixed region are negligible. Note that the presence of Clark and Peltier's low-Richardson-number critical layer is implicitly used in the

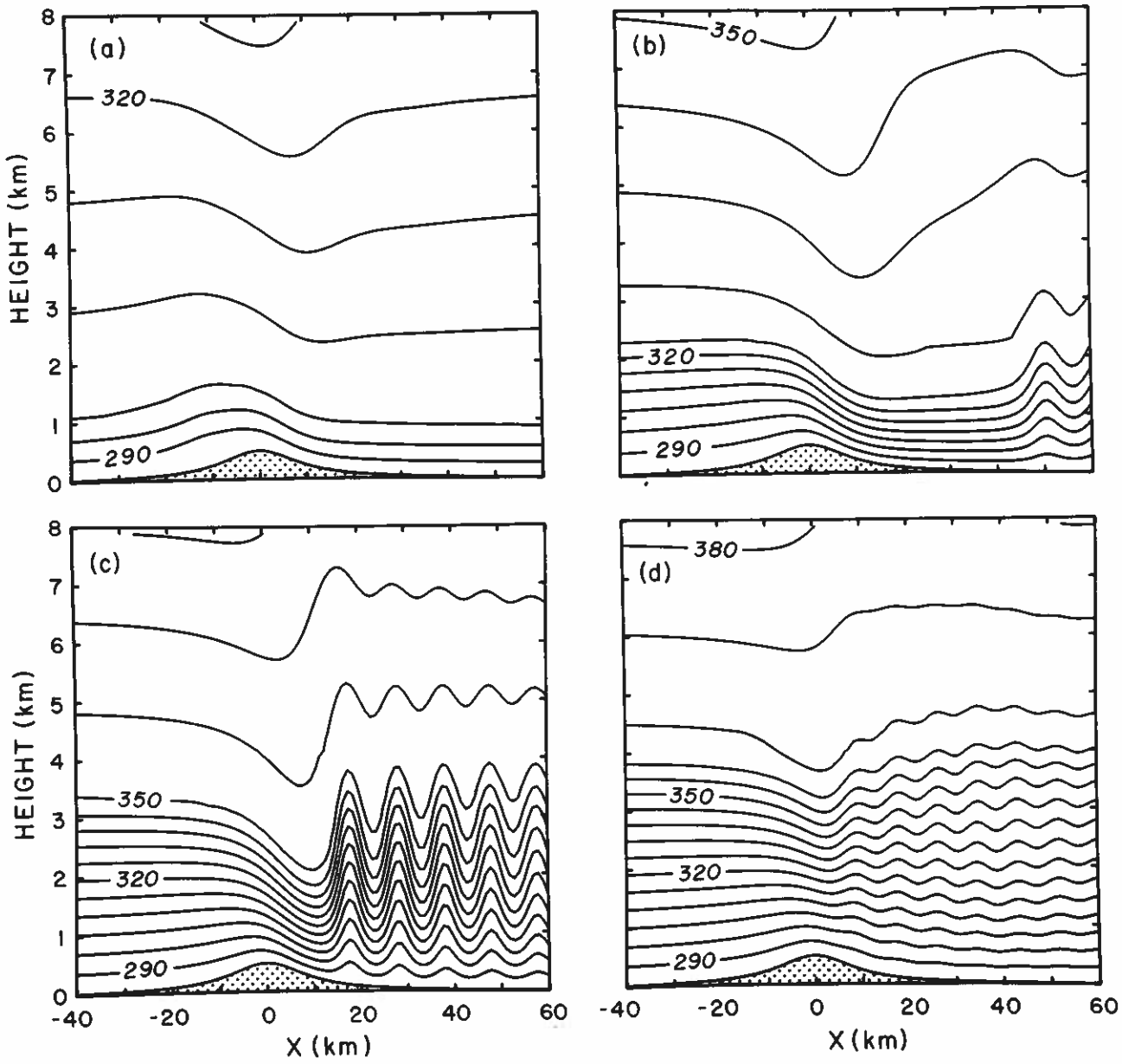

FIG. 4.8. Isentropes for the airflow in a two-layer atmosphere at $u_0 t/a = 25$, when $N_L h_m/u_0 = 0.5$ and the interface is at (a) u_0/N_L; (b) $2.5u_0/N_L$; (c) $3.5u_0/N_L$; (d) $4u_0/N_L$. (From Durran 1986a.)

derivation of Smith's upper boundary condition, since without the critical layer, pressure perturbations would not be negligible at the top of the well-mixed region (unless the well-mixed region was unrealistically deep).

Although the theories of Peltier and Clark, and of Smith, might both be considered theoretical descriptions of the flow beneath a low-Richardson-number ($\mathrm{Ri} < \frac{1}{4}$) critical layer, significant differences in the mathematical formulation of each theory lead to very different results. Peltier and Clark (1983) solved the time-dependent linear wave equations subject to a linearized free-surface condition (i.e., a fixed horizontal boundary that reflects all incoming waves with a 180° phase shift), whereas Smith solved Long's equation for the finite-amplitude steady-state flow beneath a deformable upper boundary along which the wind speed was constant. Peltier and Clark's results imply that a low-Richardson-number critical layer will produce amplification only when it is positioned approximately $\frac{1}{4} + n/2$, $n = 0, 1, \ldots$ vertical wavelengths above the topography. On the other hand, Smith's results suggest

amplification is possible over the entire range of critical-layer heights between $(\frac{1}{4} + n)$ and $(\frac{3}{4} + n)$ vertical wavelengths. Given the presence of a suitably located low-Richardson-number critical level, the amplification process proposed by Peltier and Clark is independent of mountain height. (Note, however, that when the critical level is "self-induced" by wave breaking, the development of the critical level, and hence the basic structure of the total flow, can be very sensitive to mountain height.) In contrast, the results of Smith are explicitly dependent on mountain height in a manner similar to conventional, shallow-water hydraulic theory.

Durran and Klemp (1987) and Bacmeister and Pierrehumbert (1988) used these differences to conduct a series of numerical experiments testing each theoretical model of the wave-breaking process. These investigators examined the response of air flowing over a mountain to changes in the mountain height and changes in the height of a critical layer in the mean flow. In most of the cases examined by Durran and Klemp, and Bacmeister and Pierrehumbert, a local region of turbulent flow forms over the mountain where the mountain wave interacts with the mean-state critical layer. (To be specific, Durran and Klemp found that significant regions of Ri $< \frac{1}{4}$ developed above the mountain in all simulations with the critical layer located between $\frac{1}{4}$ and $\frac{3}{4}$ vertical wavelengths above the ground, whenever Nh/U exceeded 0.2.) Thus, although the wave-breaking theories of Peltier and Clark, and of Smith, were originally formulated to describe the flow field beneath a region of wave breaking, they should also apply to the cases with a mean-state critical layer studied by Durran and Klemp, and Bacmeister and Pierrehumbert.

In accordance with Smith's theory, Durran and Klemp, and Bacmeister and Pierrehumbert found a high amplitude response could be obtained if the critical layer was located anywhere between $\frac{1}{4}$ and $\frac{3}{4}$ vertical wavelengths above the ground. They also found a dependence on mountain height closely paralleling the predictions of Smith. A representative example of these simulations is shown in Fig. 4.9. In the case illustrated in Fig. 4.9, the mean stability is constant everywhere, and the wind speed is constant between the ground and 5 km, and zero in the region above 7 km. The two regions of constant wind speed are connected by a layer with linear wind shear between 5 and 7 km. The mean Richardson number in the shear layer is 1.1; however, in both cases a region of stagnant flow develops over the mountain in which the local Richardson number is less than $\frac{1}{4}$.

Following Peltier and Clark, the critical layer in Fig. 4.9 would be estimated to lie $\frac{7}{12}$ of a vertical wavelength above the ground. This is far from the resonant level of $\frac{9}{12}$ vertical wavelength, and thus should not permit the development of a large-amplitude response. Nevertheless, as shown in Fig. 4.9b, a large response does develop when $Nh_m/u_0 = 0.4$. Turning to Smith's theory, a reasonable choice for the height of the dividing streamline would be the middle of the shear layer, or $\frac{6}{12}$ of a vertical wavelength above the ground. Smith's theory predicts that, if the dividing streamline is fixed at this location and the mountain height is gradually increased, the flow should undergo a change from weak waves to a large-amplitude response

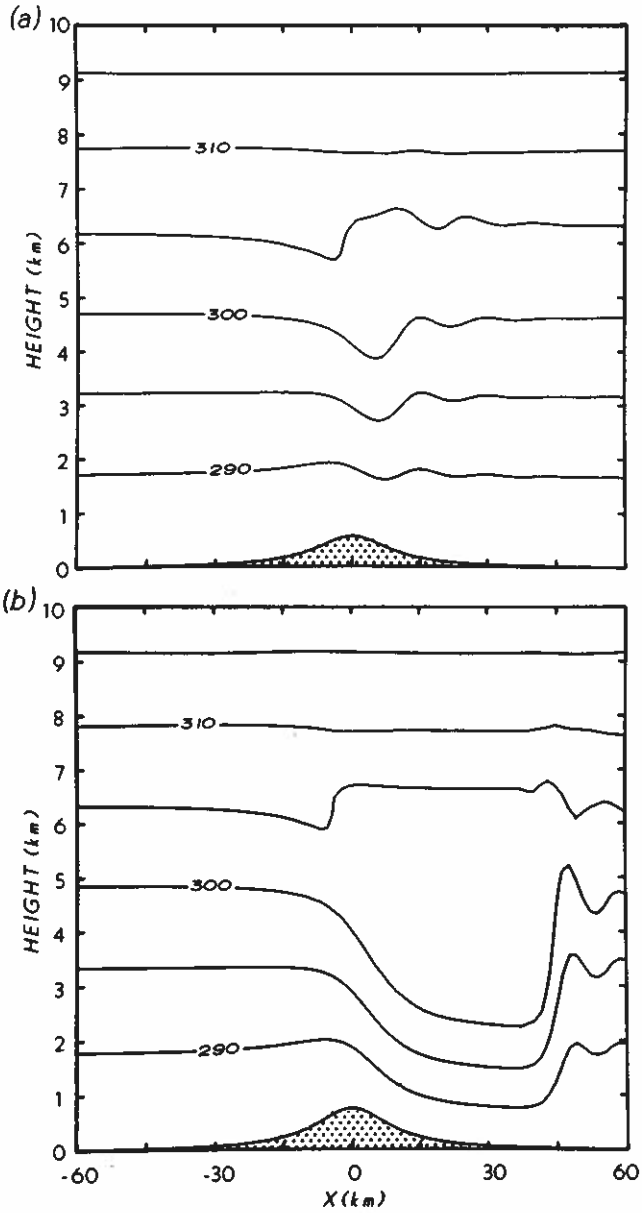

FIG. 4.9. Isentropes for a flow with a critical layer at $\frac{7}{12}$ of a vertical wavelength (dividing streamline at approximately $\frac{1}{2}$ vertical wavelength) when Nh_m/u_0 is (a) 0.3 and (b) 0.4. (From Durran and Klemp 1987.)

when Nh_m/u_0 exceeds a critical value between 0.3 and 0.4; a result that agrees with the numerical simulations shown in Figs. 4.9a,b. Other simulations, conducted by Durran and Klemp, and Bacmeister and Pierrehumbert over a wide variety of different situations, confirm the ability of Smith's theory to adequately describe topographically disturbed flow in an airstream with a mean critical layer. These simulations do not support the linear resonance mechanism of Clark and Peltier.

The most significant aspect of the recent work by Smith, Durran and Klemp, and Bacmeister and Pierrehumbert is not a demonstration of the importance of wave breaking, which had been previously provided by Clark and Peltier, but an elucidation of the connection between wave breaking and the hydraulic amplification mechanism. Durran and Klemp (1987) have shown that Smith's solution satisfies

$$(1 - \mathcal{F}^{-2})\frac{\partial(D + h)}{\partial x} = \frac{\partial h}{\partial x}, \tag{4.37}$$

where

$$\mathcal{F}^2 = \frac{1 - (N\delta_c/u_0)\sin(ND/u_0)}{1 - \cos(ND/u_0)}. \tag{4.38}$$

Here $D(x)$ is the total depth of the fluid between the dividing streamline and the topography, $\delta_c(x)$ is the displacement of the dividing streamline from its undisturbed height upstream, and N and u_0 represent the constant values of Brunt–Väisälä frequency and cross-mountain wind speed below the critical-level in the undisturbed upstream flow. The parameter $\mathcal{F}$ is analogous to the conventional shallow-water Froude number; in particular it renders (4.37) equivalent to (4.33), and both $\mathcal{F} = 1$ and $\mathrm{Fr} = 1$ imply that the phase speed of the most rapidly propagating linear gravity wave in each respective system is equal to the speed of the mean flow. However, the dynamics that determine $\mathcal{F}(x)$ and $\mathrm{Fr}(x)$ are somewhat different. As a consequence, the shallow-water system does not provide an exact model of Smith's stratified flow, even when $D(-\infty)$ and $h(x)$ are identical and $\mathcal{F}(-\infty) = \mathrm{Fr}(-\infty)$; i.e., the two fluids will not undergo exactly the same thickness change, $D(x)$, as they traverse the obstacle. However, as discussed by Durran and Klemp, there is reasonable quantitative agreement between the two systems when the depth of the stratified flow is less than one-half vertical wavelength. At larger values of D the internal perturbations in the stratified fluid can produce significant quantitative differences, but a qualitative similarity remains.

In order to use Smith's hydraulic theory to predict the steady-state flow over a mountain, it is necessary to specify the initial height of the dividing streamline, $D(-\infty)$. In a case with a mean-state critical layer, Durran and Klemp (1987) and Bacmeister and Pierrehumbert (1988) have shown that good results can be obtained by setting $D(-\infty)$ equal to the height of the critical layer. However, in the case of breaking waves and wave-induced critical layers, no height for the dividing streamline can be specified a priori. Consequently, the application of the hydraulic model to breaking waves is limited to a posteriori diagnosis; it cannot be used to predict the final steady state or the flow evolution. Nevertheless, the successful a posteriori application of hydraulic theory to the case of breaking waves allows one to construct a simple unified model for the creation of high lee-slope fluid velocities in a wide range of geophysical flows, including the flow of water over a rock, the flow of a multilayered airstream over a mountain (without wave breaking), the flow of a single-layered airstream over a mountain when breaking waves are present, and cross-mountain flow bounded above by a mean-state critical layer. That simple unified model consists of a two-part amplification process. In the first part of the amplification process, high fluid velocities are produced near the obstacle's crest as pressure gradient forces in a standing gravity wave dominate the force balance on fluid parcels in the upstream flow. Fluid near the crest experiences a net acceleration and a net elevation gain (as in subcritical shallow-water flow). The second part of the amplification process only occurs if the obstacle is sufficiently high, in which case the gravity-wave-induced acceleration becomes so great that it is impossible to develop a lee-side pressure gradient capable of decelerating the flow (as in supercritical shallow-water flow). In this circumstance, the flow undergoes a transition; the force balance on a fluid parcel is dominated by gravity, and very high velocities develop as the fluid accelerates down the lee slope like a hockey puck descending a mound of ice.

4.4.4. Forecasting downslope winds

As discussed in the preceding sections, there appears to be a fundamental dynamical similarity between the development of downslope winds in the atmosphere and the development of supercritical flow in a hydraulic jump. This is not a new idea, nor is it one that has provided much practical assistance to forecasters in the past. Indeed, one might suppose that if the simple hydraulic analog introduced by Long in the early 1950s had led to a set of highly successful forecasting guidelines, the alternative mechanisms proposed to explain the development of strong downslope winds would not have enjoyed much popularity.

One problem with any attempt to apply shallow-water hydraulic theory directly to the problem of downslope wind forecasting is that there appear to be at least three rather different circumstances in which the atmosphere

can undergo a transition from subcritical to supercritical flow. These three circumstances are:

1) *Wave breaking:* as in an atmosphere with constant N and u_0 where the mountain is large enough to force breaking waves (Clark and Peltier 1977).

2) *Scorer-parameter layering:* as in an atmosphere with constant u_0, and a two-layer structure in N where the mountain is too small to force breaking waves (Durran 1986a).

3) *Capping by a mean-state critical layer:* as in an atmosphere with constant N and u_0 below a critical layer, where in the absence of the critical layer, the mountain is too small to force breaking waves (Smith 1985a).

Until more detailed guidance is developed, the forecaster might do well to examine the observed or forecast atmospheric sounding for factors that would promote the development of atmospheric hydraulic jumps through the action of one of the preceding three processes.

In a case where there is a deep cross-mountain flow and no mean-state critical layer (as in most of the Boulder, Colorado and Owens Valley, California windstorms), observational evidence suggests that conditions favorable for downslope winds occur when:

(i) The wind is directed across the mountain (roughly within 30° of perpendicular to the ridgeline) and the wind speed at mountaintop level exceeds a terrain dependent value of 7 to 15 m s^{-1}.

(ii) The upstream temperature profile exhibits an inversion or a layer of strong stability near mountaintop level (Colson 1954; Brinkmann 1974).

These factors would favor the development of strong winds by creating conditions similar to situation 2). In addition they promote the development of larger amplitude mountain waves and thereby increase the chances for breaking waves; i.e., situation 1). Breaking waves are also favored when the upper-tropospheric winds are not excessively strong. Thus, cross-mountain wind speeds of 30 to 40 m s^{-1} may be more likely to produce strong downslope winds than the higher values observed near the axis of the jet stream.

In cases where there is a mean-state critical layer in the flow above mountaintop level (e.g., many Yugoslavian boras and "canyon winds" on the western side of the Wasatch Front in Utah), criterion (i) still applies. There is likely to be an inversion near the critical level, but the critical level itself appears to be more important than the inversion in the generation of strong-downslope winds. However, even when a mean-state critical level is present it may not be the feature that is primarily responsible for the development of downslope winds. Klemp and Durran (1987) conducted numerical simulations suggesting that the 15 April 1982 bora, observed during ALPEX (the Alpine Experiment), was produced by simple wave breaking below a mean-state critical layer [i.e., situation 1)] and that the development of strong surface winds was not inhibited by the absence of the mean-state critical layer.

Additional factors that may influence the strength of a given wind event are the terrain shape, atmospheric humidity, and the time of day. Long mountain ridges with gentle windward slopes and steep lee slopes are most favorable for the generation of strong downslope winds (Smith 1977; Lilly and Klemp 1979; Hoinka 1985). High relative humidity in the lower troposphere appears to reduce the strength of windstorms (Barcilon et al. 1979; Durran and Klemp 1983). Climatological studies of windstorms in Boulder, Colorado show a distinct tendency for the highest winds to occur in the nighttime or the early morning (Whiteman and Whiteman 1974; Brinkmann 1974). This diurnal signal is probably due to a diurnal modulation of boundary-layer friction. Although they did not investigate diurnal effects, Richard et al. (1989) recently demonstrated the importance of surface friction by showing that its inclusion in a numerical model eliminates the unrealistic tendency of models with a free-slip lower boundary to form a layer of high surface wind that propagates indefinitely downstream (as in Figs. 4.8b and 4.9b).

In a case with no mean-state critical layer, the forecaster might also examine the relationship between the tropopause height and the vertical wavelength of hydrostatic mountain waves. Klemp and Lilly (1975) found the strongest downslope wind events occurred in Boulder when a one-half wavelength phase shift was present between the ground and the tropopause. The theoretical support for this relationship rests on the partial reflection mechanism of linear theory; however, as discussed in section 4.4.2, the application of this theory to finite-amplitude waves can produce misleading results. It is therefore not entirely clear why the phase-shift correlation is as high as it seems. Although the strongest Boulder windstorms seem to exhibit the half-wavelength phase shift, exclusive reliance on phase shift and wind speed/direction criteria can lead to the prediction of windstorms when none actually occur. Bower and Durran (1986) discuss a nonwindstorm event that did satisfy the half-wavelength phase shift criteria, along with appropriate conditions on the wind speed and direction. Unlike other windstorm cases, the lower tropospheric stability in the nonwindstorm case was very weak and there was no significant inversion near mountaintop level. On the basis of the climatologies of Brinkmann (1974) and Colson (1954) one might suppose that the absence of low-level stability was responsible for the failure of a downslope wind to develop in Bower and

Durran's "well-tuned" cross-mountain flow. Further support for the idea that lower tropospheric stability plays an important role in Boulder windstorms has been provided by numerical simulations of the 11 January 1972 windstorm. Durran (1986a) showed that the development of the windstorm (including wave breaking in the upper troposphere) was triggered by the formation of a hydraulic-jump-like disturbance in an elevated inversion near mountaintop level. As shown in Figs. 4.10a,b, no windstorm developed when the numerical simulation was repeated using a modified upstream sounding from which the elevated inversion had been removed. In summary, it is possible that the half-wavelength criteria may be a necessary condition for the strongest Boulder windstorms, but it does not appear to be a sufficient criteria for even a moderate storm.

4.4.5. Gustiness near the surface in downslope winds

In many downslope windstorms, the surface wind is very gusty. An example of this gustiness is shown in Fig. 4.11, the anemometer trace recorded at the National Center for Atmospheric Research during the onset of the 17 January 1982 Boulder windstorm. Gusts in excess of 210 km h^{-1} (58 m s^{-1}) with lulls of less than 15 km h^{-1} (4 m s^{-1}) are evident after the onset of this severe storm (time reads right to left in Fig. 4.11). Fluctuations with a period of slightly more than one minute appear to dominate the surface wind observations. In addition to the surface data, observations of the gust structure a few hundred meters above the surface have recently been obtained by Neiman et al. (1988) using a pulsed Doppler lidar; an example of their analysis appears in Fig. 4.12. These observations, taken during a moderate Boulder, Colorado windstorm, show a series of gusts forming at the upwind edge of the observation area and maintaining their coherence as they propagate downstream at the approximate speed of the mean winds. The dominant period of these fluctuations is approximately 4 minutes; the maximum and minimum velocities are roughly 34 and 16 m s^{-1}. The gustiness observed above the surface by Neiman et al. is less extreme than that recorded in the preceding surface anemometer trace. Some of the difference can be attributed to differences in the strength of the two windstorms; however, an additional enhancement in the surface gustiness is probably produced by surface friction.

Clark and Farley (1984) investigated gustiness in the 11 January 1972 windstorm using two- and three-dimensional numerical models. The two-dimensional simulations did not appear to produce gusty surface winds. The three-dimensional simulations were nominally similar to those in two-dimensions, because there were no variations in the topography or the mean atmospheric structure

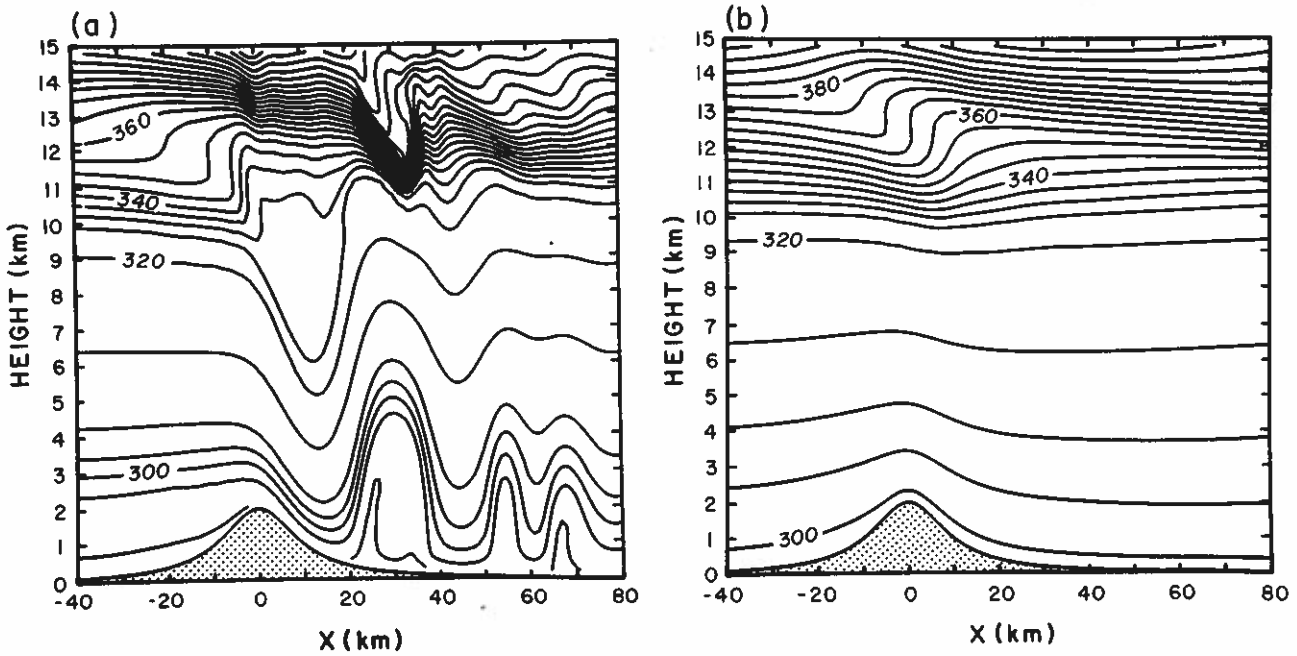

FIG. 4.10. (a) Isentropes form a simulation of the 11 January 1972 Boulder windstorm using the upstream conditions observed at Grand Junction, at a model time of 12 000 s. (b) As in (a), except that the upstream sounding has been modified to remove the elevated inversion. (From Durran 1986a.)

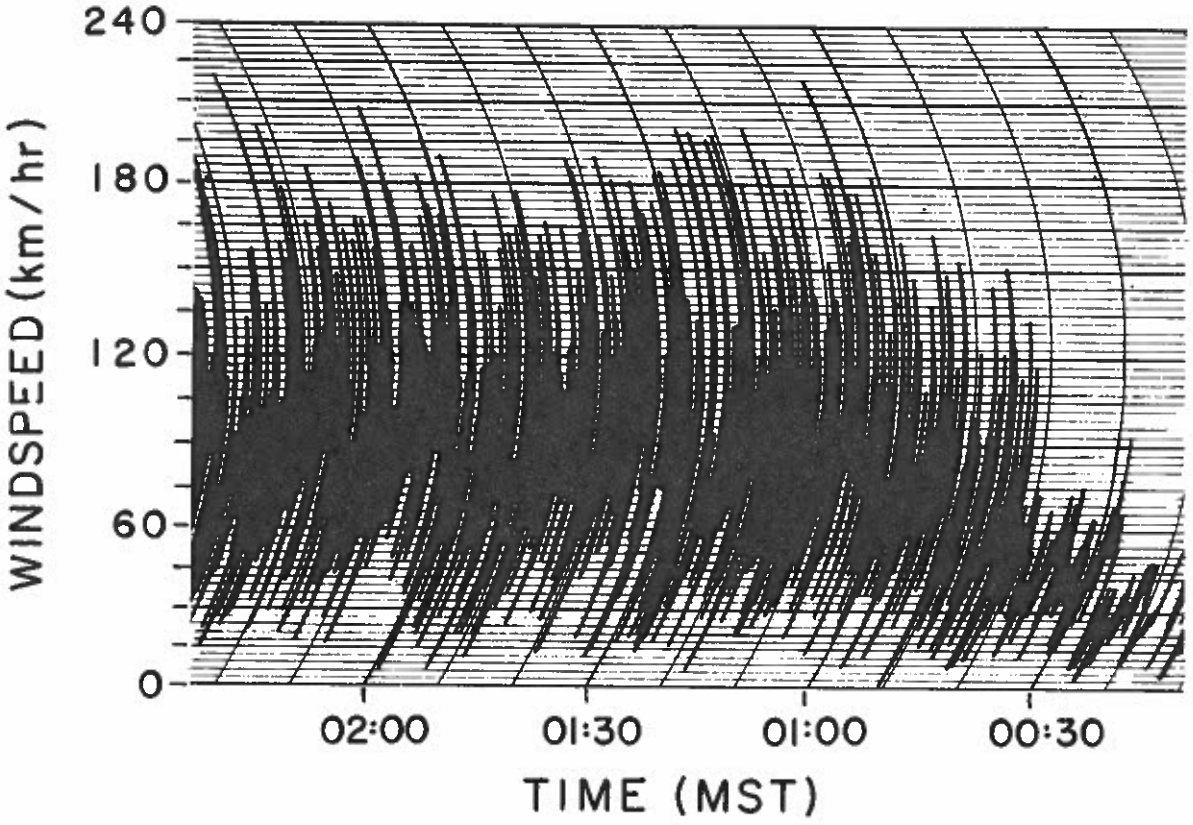

FIG. 4.11. Anemometer trace recorded at the National Center for Atmospheric Research during the onset of the 17 January 1982 Boulder windstorm. Time reads from right to left.

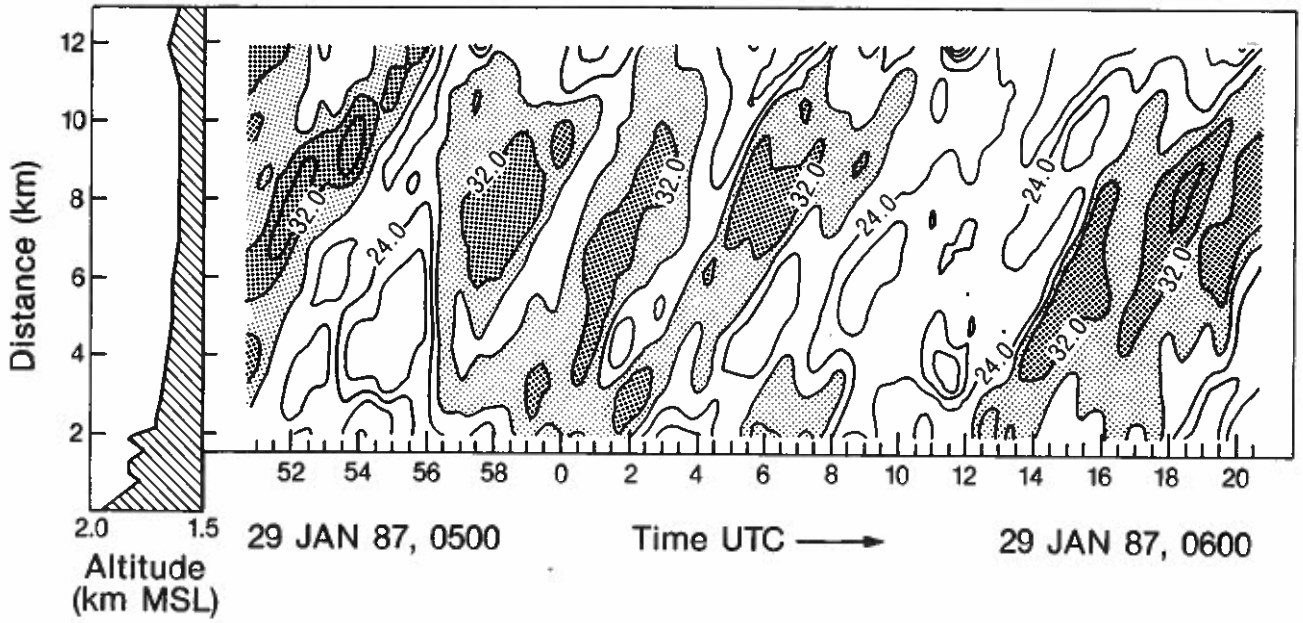

FIG. 4.12. Range–time display of Doppler-lidar-measured radial velocities (m s^{-1}) on 29 January 1987 in the vicinity of Boulder, Colorado. The lidar was located in the foothills and pointed eastward, out of the mountains at an elevation angle of −2°. The optical beam intersected the ground 12 km downrange. The terrain profile underneath the lidar beam is displayed along the vertical axis. (From Neiman et al. 1988.)

along the direction parallel to the ridge. Clark and Farley tested the stability of two-dimensional flow to three-dimensional perturbations by applying a small random three-dimensional forcing to the potential temperature field in the three-dimensional simulations. They found that the three-dimensional flow was stable with respect to these perturbations until the waves began to overturn. In the wave-breaking region, the random three-dimensional forcing triggered unstable disturbances that eventually penetrated to the surface and produced gusty winds along the lee slope. Clark and Farley suggested that this gustiness is produced by a competition between wave buildup via forced gravity wave dynamics and wave breakdown via convective instability. Figure 4.13 provides an example of the surface wind variation at one point on the lee slope in Clark and Farley's three-dimensional simulation. The dominant period of these fluctuations is approximately 8 minutes; the maximum and minimum velocities during the gusty period are approximately 70 and 50 m s^{-1}. Clark and Farley have hypothesized that better numerical resolution would reduce the period of the gusts in their simulation, which could bring it into closer agreement with the measurements of Nieman et al. (1988).

Given the crudeness with which the topography and boundary processes are represented in their model, and the fact that they were not attempting to simulate the case observed by Nieman et al., Clark and Farley's simulation appears to provide a qualitatively correct description of the gustiness in the flow; however, Scinocca and Peltier (1989) have recently found that realistic gust structures can be produced in high resolution simulations of strictly two-dimensional flow. Kuo (1963) has shown that small-amplitude perturbations in a stably stratified unidirectional shear flow grow most rapidly when the perturbations are two-dimensional, but that when the same flow is unstably stratified the most rapidly growing modes are three-dimensional. The basic state in which the gusts appear to develop in the simulations of Clark and Farley, and Scinocca and Peltier contains both stably and unstably stratified subregions. It is therefore not obvious whether two-dimensional or three-dimensional perturbations should be expected to grow most rapidly. Further research is needed to determine the relative importance of two-dimensional and three-dimensional circulations in gust generation.

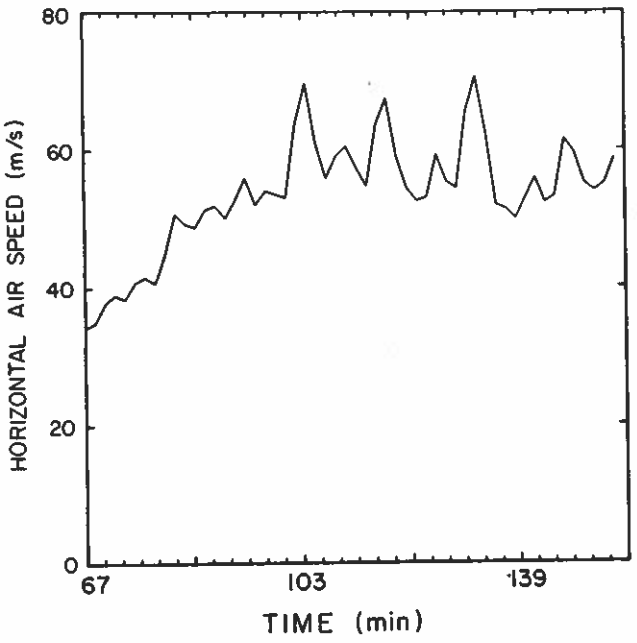

FIG. 4.13. Time series plot of the horizontal wind speed 9.5 km downwind of the ridge crest in a three-dimensional simulation of the 11 January 1972 Boulder, Colorado windstorm. (From Clark and Farley 1984.)

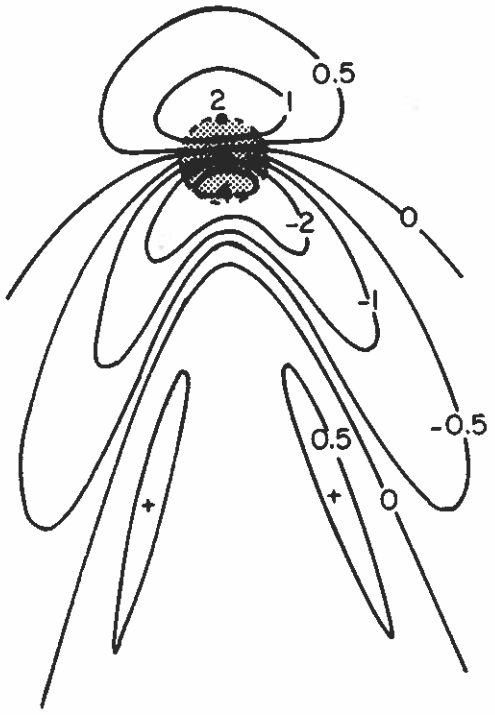

FIG. 4.14. Horizontal cross-section of the vertical displacement field in hydrostatic flow over a circular bell-shaped mountain of the form (4.39). The cross section is at an elevation of $\frac{1}{4}$ vertical wavelength. Shading indicates the topography within a radial distance a from the peak. (From Smith 1980.)

4.5. Flow over isolated mountains

The preceding sections have focused on the case of flow over an infinitely long mountain barrier, with no variations in the direction parallel to the ridge axis. Most real mountains are highly three-dimensional, and unfortunately our current understanding of the flow around three-dimensional mountains is far from complete. Significant

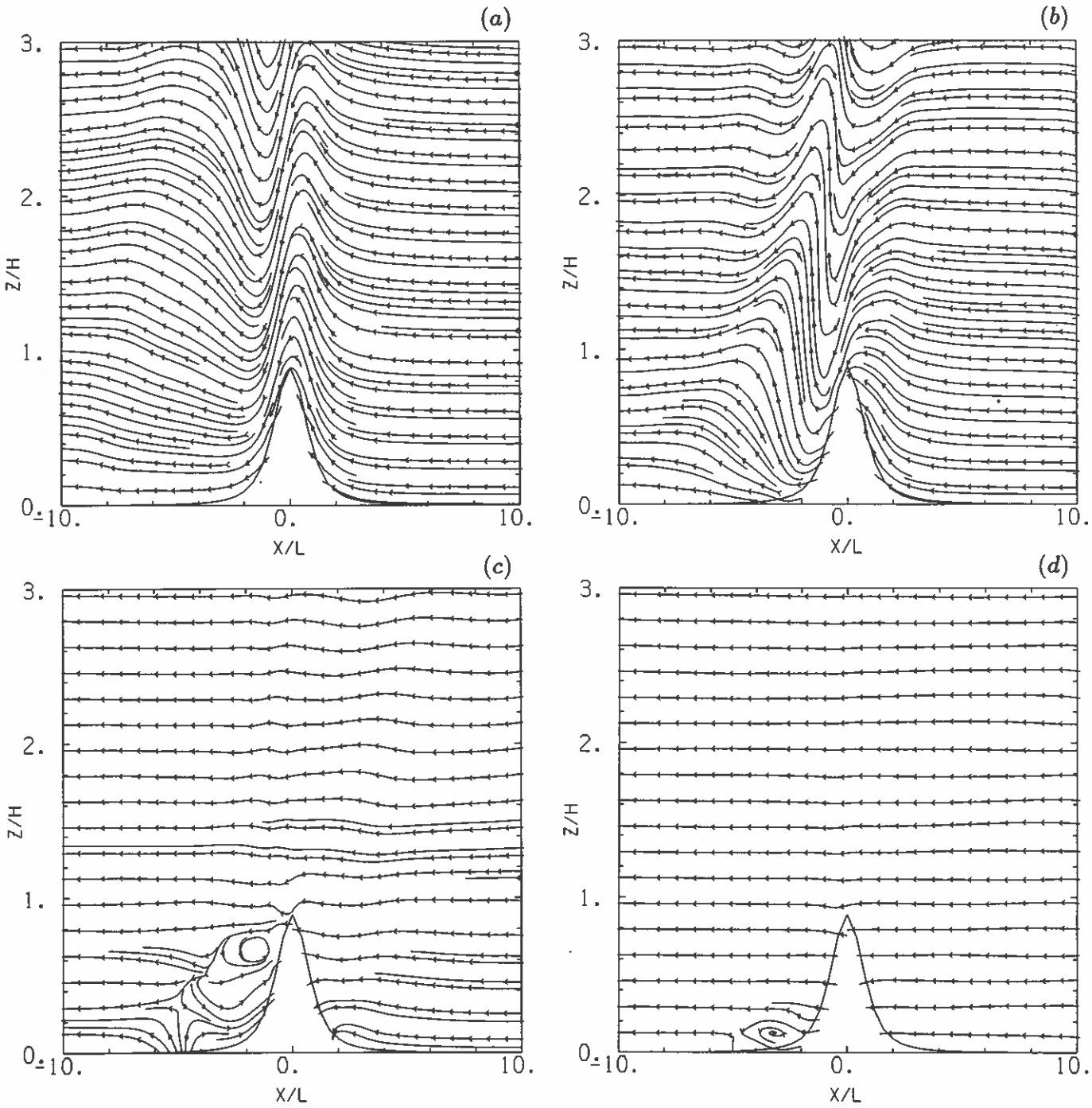

FIG. 4.15. Streamlines in the x–z plane through the center of a circular bell-shaped mountain, when the upstream value of Nh_m/u_0 is (a) 0.45, (b) 1.5, (c) 4.5, (d) 18. Airflow is from the right to the left. (From Smolarkiewicz and Rotunno 1989.)

progress has been made, however, in one case of relatively simple three-dimensional geometry—the isolated circular mountain. A discussion of the airflow over circular mountains and hills is presented by Carruthers and Hunt, Chapter 5, and in reviews by Smith (1979) and Queney et al. (1960). An analysis of the circumstances under which air diverts around a mountain, instead of flowing over it, appears in the Appendix to Chapter 5 (Smith). In the following section we will limit our attention to some recent results describing the dynamics of flow

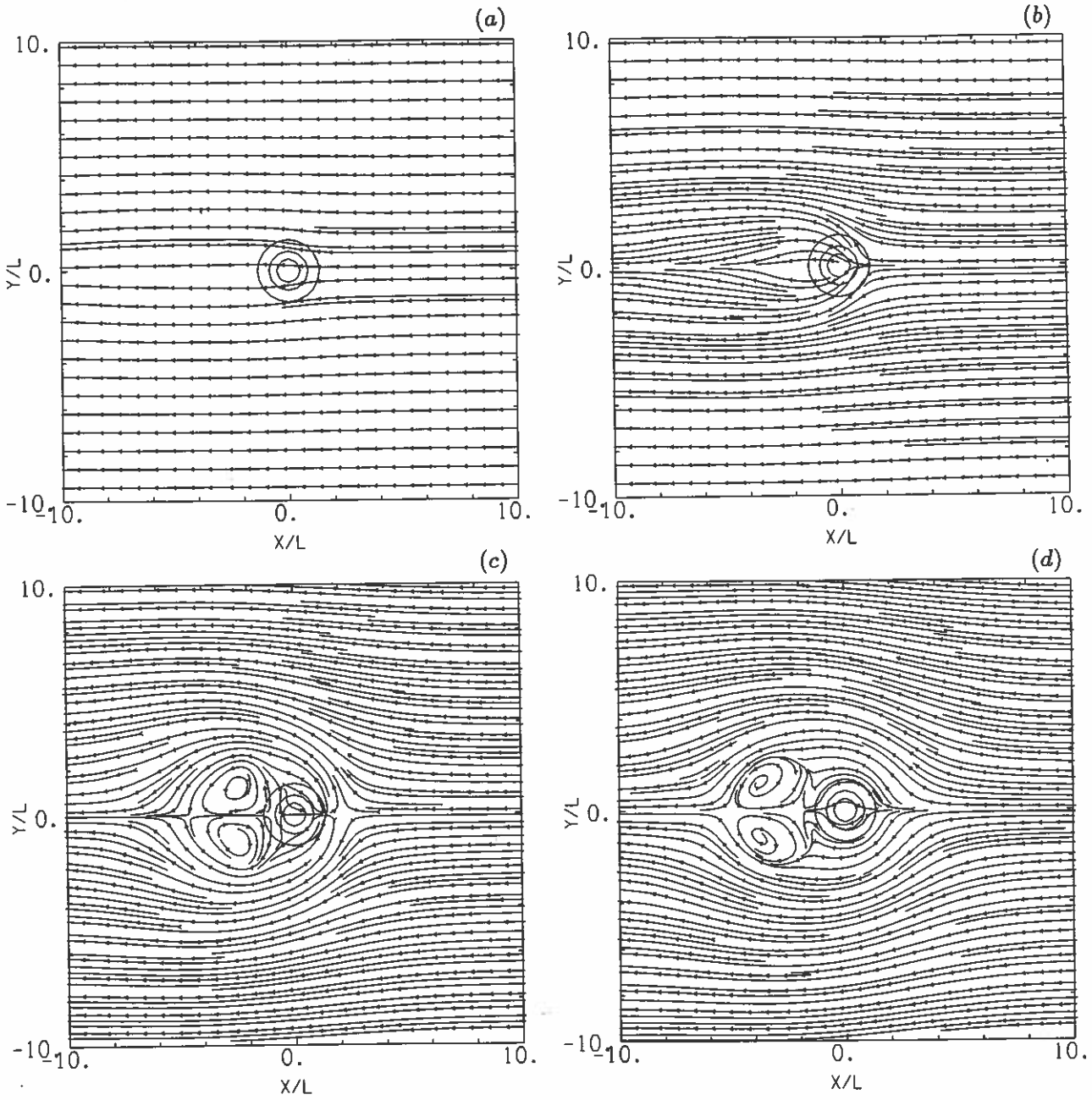

FIG. 4.16. As in Fig. 4.15, except that the streamlines are displayed in the x–y plane and represent the flow on the surface of the topography. (From Smolarkiewicz and Rotunno 1989.)

around a circular obstacle when the mean wind speed and stability are constant with height.

Smith (1980) obtained linear solutions for waves in an atmosphere with constant N and u_0 flowing over a bell-shaped circular mountain

$$h(x, y) = \frac{h_m}{[(x^2 + y^2)/a^2 + 1]^{3/2}}, \qquad (4.39)$$

where h_m and a are the height and horizontal scale of the mountain. An example of Smith's solution for the wave-induced vertical displacement at a level one-quarter wavelength above the surface is shown in Fig. 4.14. The flow in Fig. 4.14 is hydrostatic ($Na/u_0 \gg 1$); yet unlike the hydrostatic waves forced by a two-dimensional mountain, the disturbance is not confined to the region directly over the mountain. Instead, the perturbations are

concentrated along parabolas extending downstream from the mountain.

Smith's solutions are based on linearized equations and are formally valid only in the limit $Nh_m/u_0 \ll 1$. In the opposite limit, $Nh_m/u_0 \gg 1$ the behavior is similar to two-dimensional potential flow in a horizontal plane where all the fluid is diverted laterally around the mountain (Drazin 1961). Analytic models are not available to describe the flow when Nh_m/u_0 is of order unity. Smolarkiewicz and Rotunno (1989) bridged this theoretical gap by calculating a series of numerical solutions for the flow around the circular bell mountain (4.39); their results are illustrated in Figs. 4.15 and 4.16, which represent steady or quasi-steady solutions. Streamlines in a vertical cross-section through the center of the hill are shown in Fig. 4.15. The case $Nh_m/u_0 = 0.45$ (Fig. 4.15a) is in quantitative agreement with Smith's linear theory; qualitative agreement remains at $Nh_m/u_0 = 1.5$ (Fig. 4.15b). However, a major change in the flow regime occurs as Nh_m/u_0 is increased to 4.5 (Fig. 4.15c). The vertically propagating gravity waves evident at $Nh_m/u_0 = 1.5$ are virtually eliminated and closed circulations develop in the lee of the mountains. When $Nh_m/u_0 = 18$ (Fig. 4.15d), the flow is largely horizontal. Figure 4.16 shows a plot of the surface streamlines associated with each of the four cases in Fig. 4.15. Note that as the flow becomes more nonlinear, there is an increased lateral displacement of the flow around the mountain. Closed vortices appear in the lee of the mountain in the two simulations with the highest values of Nh_m/u_0.

Satellite imagery has revealed vortices downstream of isolated mountains in the atmosphere. Lee vortices have also been observed in laboratory experiments (Hunt and Snyder 1980). The development of these vortices has traditionally been explained by analogy with the flow of a homogeneous fluid past a cylinder, where vorticity is generated by surface friction in the viscous boundary layer and advected downstream after the boundary layer separates from the obstacle. This mechanism cannot be responsible for the development of the lee vortices in Smolarkiewicz and Rotunno's simulations, however, because those simulations were conducted without surface friction. Yet the vorticity apparent in Figs. 4.16c,d had to be created by some process because there was no vorticity in the upstream flow (N and u_0 were constant). Smolarkiewicz and Rotunno have suggested that the lee vortices were generated in their simulations through a three-step process. First, as the stratified flow is disturbed by the mountain, horizontal density gradients are produced. Second, these horizontal density gradients baroclinically generate horizontal vorticity. Third, the sharply descending flow in the lee of the mountain redistributes the horizontal vorticity into the vertical by tilting and stretching the vortex filaments. Since the depth of the surface boundary layer is often small compared with the height of a large mountain, it is likely that this inviscid baroclinic vorticity-generation mechanism is responsible for the generation of many of the lee vortices observed in the atmosphere. Smolarkiewicz et al. (1988) have successfully applied the numerical model to the simulation of airflow around the island of Hawaii.

Acknowledgments. This effort was supported by NSF Grant ATM-8796281.

REFERENCES

Bacmeister, J.T. and R.T. Pierrehumbert, 1988: On high-drag states of nonlinear flow over an obstacle. *J. Atmos. Sci.*, **45**, 63-80.

Barcilon, A., J.C. Jusem, and P.G. Drazin, 1979: On the two-dimensional hydrostatic flow of a stream of moist air over a mountain ridge. *Geophys. Astrophys. Fluid Dynamics*, **13**, 125-140.

Blumen, W.; 1965: A random model of momentum flux by mountain waves. *Geofys. Publ*, **26**, 1-33.

Bower, J.B., and D.R. Durran, 1986: A study of wind profiler data collected upstream during windstorms in Boulder, Colorado. *Mon. Wea. Rev.*, **102**, 592-602.

Brinkmann, W.A.R., 1974: Strong downslope winds at Boulder, Colorado. *Mon. Wea. Rev.*, **102**, 592-602.

Clark, T.L. and R.D. Farley, 1984: Severe downslope windstorm calculations in two and three spatial dimensions using anelastic interactive grid nesting: a possible mechanism for gustiness. *J. Atmos. Sci.*, **41**, 329-350.

———, and W.R. Peltier, 1977: On the evolution and stability of finite-amplitude mountain waves. *J. Atmos. Sci.*, **34**, 1715-1730.

———, and ———, 1984: Critical level reflection and the resonant growth of nonlinear mountain waves. *J. Atmos. Sci.*, **41**, 3122-3134.

Colson, DeVer, 1954: Meteorological problems in forecasting mountain waves. *Bull. Amer. Meteor. Soc.*, **35**, 363-371.

Drazin, P.G., 1961: On the steady flow of a fluid of variable density past an obstacle. *Tellus*, **13**, 239-251.

Durran, D.R.; 1986a: Another look at downslope windstorms. Part I: On the development of analogs to supercritical flow in an infinitely deep, continuously stratified fluid. *J. Atmos. Sci.*, **43**, 2527-2543.

———; 1986b: Mountain waves. *Mesoscale Meteorology and Forecasting*, P. Ray ed., Boston, American Meteorological Society, 472-492.

———, and J.B. Klemp; 1983: A compressible model for the simulation of moist mountain waves. *Mon. Wea. Rev.*, **111**, 2341-2361.

———, and ———: 1987: Another look at downslope winds. Part II: Nonlinear amplification beneath wave-overturning layers. *J. Atmos. Sci.*, **44**, 3402-3412.

Eliassen, A. and E. Palm, 1960: On the transfer of energy in stationary mountain waves. *Geofys. Publ.*, **22**, 1-23.

Gill, A.E., 1982: *Atmosphere-Ocean Dynamics*. Academic Press, New York, 662 pp.

Hoinka, K.P., 1985: A comparison of numerical simulations of hydrostatic flow over mountains and observations. *Mon. Wea. Rev.*, **113**, 719-735.

Holton, J.R., 1979: *An Introduction to Dynamic Meteorology, 2nd Ed.* Academic Press, New York, 391 pp.

Houghton, D.D. and A. Kasahara, 1968: Nonlinear shallow fluid flow over an isolated ridge. *Comm. Pure and Appl. Math.*, **21**, 1-23.

Hunt, C.R., and W.H. Snyder, 1980: Experiments on stably and neutrally stratified flow over a model three-dimensional hill. *J. Fluid Mech.*, **96**, 671-704.

Klemp, J.B. and D.R. Durran, 1987: Numerical modelling of Bora winds. *Meteorol. Atmos. Phys.*, **36**, 215-227.

———and D.K. Lilly, 1975: The dynamics of wave induced downslope winds. *J. Atmos. Sci.*, **32**, 320-339.

Kuo, H.L., 1963: Perturbations of plane Couette flow in stratified fluid and origin of cloud streets. *Phys. Fluids*, **6**, 195-211.

Lilly, D.K., and J.B. Klemp, 1979: The effects of terrain shape on nonlinear hydrostatic mountain waves. *J. Fluid Mech.*, **95**, 241-261.

Long, R.R., 1953a: A laboratory model resembling the "Bishop-wave" phenomenon. *Bull. Amer. Meteor. Soc.*, **34**, 205-211.

———, 1953b: Some aspects of the flow of stratified fluids. I. A theoretical investigation. *Tellus*, **5**, 42-58.

———, 1954: Some aspects of the flow of stratified fluids. II. Experiments with a two fluid system. *Tellus*, **6**, 97-115.

Neiman, P.J., R.M. Hardesty, M.A. Shapiro, and R.E. Cupp, 1988: Doppler lidar observations of a downslope windstorm. *Mon. Wea. Rev.*, **116**, 2265-2275.

Peltier, W.R., and T.L. Clark, 1979: The evolution and stability of finite-amplitude mountain waves. Part II. Surface wave drag and severe downslope windstorms. *J. Atmos. Sci.*, **36**, 1498-1529.

———, and ———, 1983: Nonlinear mountain waves in two and three spatial dimensions. *Quart. J. Roy. Meteor. Soc.*, **109**, 527-548.

Queney, P. 1948: The problem of air flow over mountains: a summary of theoretical studies. *Bull. Amer. Meteor. Soc.*, **29**, 16-26.

———, G. Corby, N. Gerbier, H. Koschmieder and J. Zierep, 1960: *The Airflow Over Mountains*. WMO Tech. Note 34, 135 pp.

Richard, E., P. Mascart, and E.C. Nickerson, 1989: On the role of surface friction in downslope windstorms. *J. Appl. Meteor.*, in press.

Scinocca, J.F. and W.R. Peltier, 1989: Pulsating downslope windstorms. *J. Atmos. Sci.*, in press.

Smith, R.B, 1977: The steepening of hydrostatic mountain waves. *J. Atmos. Sci.*, **34**, 1634-1654.

———, 1979: The influence of mountains on the atmosphere. *Advances in Geophysics*, Vol. 21, Academic Press, 87-230.

———, 1980: Linear theory of stratified hydrostatic flow past an isolated mountain. *Tellus*, **32**, 348-364.

———, 1985: On severe downslope winds. *J. Atmos. Sci.*, **42**,, 2597-2603.

———, 1987: Aerial observations of the Yugoslavian Bora. *J. Atmos. Sci.*, **44**, 269-297.

———, and J. Sun, 1987: Generalized hydraulic solutions pertaining to severe downslope winds. *J. Atmos. Sci.*, **44**, 2934-2939.

Smolarkiewicz, P.K., R. Rasmussen, and T.L. Clark, 1988: On the dynamics of Hawaiian cloud bands: Island forcing. *J. Atmos. Sci.*, **45**, 1872-1905.

———, and R. Rotunno, 1989: Low froude number flow past three-dimensional obstacles. Part I: Baroclinically generated lee vortices. *J. Atmos. Sci.*, in press.

Whiteman, C.D. and J.G. Whiteman, 1974: An historical climatology of damaging downslope windstorms at Boulder, Colorado. *NOAA Technical Report ERL 336-APCL 35*. Available from the Superintendent of Documents, U.S. Government Printing Office, Washington, D.C.